Applied Ocean Research 141 (2023) 103757

Contents lists available at ScienceDirect

Applied Ocean Research

journal homepage: www.elsevier.com/locate/apor

Invited paper

Numerical validations and investigation of a semi-submersible floating offshore wind turbine platform interacting with ocean waves using an SPH framework

Bonaventura Tagliafierro [a,b], Madjid Karimirad [b], Corrado Altomare [a], Malin Göteman [c], Iván Martínez-Estévez [d], Salvatore Capasso [e], José M. Domínguez [d], Giacomo Viccione [e], Moncho Gómez-Gesteira [d], Alejandro J.C. Crespo [d,*]

[a] Maritime Engineering Laboratory, Universitat Politècnica de Catalunya - Barcelona Tech, Barcelona, 84084, Spain
[b] School of Natural and Built Environment, Queen's University Belfast, Belfast, Northern Ireland, UK
[c] Department of Electrical Engineering, Uppsala University, Uppsala, Northern Ireland, Sweden
[d] Environmental Physics Laboratory, CIM-UVIGO, Universidade de Vigo, Ourense, 34002, Spain
[e] Environmental and Maritime Hydraulics Laboratory (LIDAM), University of Salerno, Fisciano, 84084, Italy

ARTICLE INFO

Keywords:
Floating wind turbine
DeepCwind
Smoothed Particle Hydrodynamics
Numerical validation
DualSPHysics
Project chrono
CFD
Incremental focused waves
Breaking waves
Vorticity

ABSTRACT

In this work, we propose numerical validations of the DeepCwind semi-submersible floating platform configuration for a single horizontal axis wind turbine using data from two experimental testing investigations. A Smoothed Particle Hydrodynamics solver is employed to estimate fluid induced loads, whereas the mooring connections are handled via an external library. The first validation setup is based on the DeepCwind offshore wind semi-submersible concept moored with a system of taut-lines and tested for free-decay surge and heave motion (OC6-Phase Ia). The damping evaluation yields a fair estimation of the heave damping behavior, whereas much more dissipation is experienced for the surge. The second validation features a full hydrodynamic characterization of the frequency-related load patterns induced by three different sea-state representations (mono-, bi-chromatic, and irregular waves) (OC6-Phase Ib). The model accurately matches the hydrodynamic load estimation for the whole spectrum of investigated wave components, perfectly capturing the non-linear behavior shown by the considered wave patterns. This work concludes with a systematic study on the motion response, mooring tension, pressure and vorticity, suggesting that: the wave steepness criterion alone cannot identify the most restrictive load case; waves with spectral characteristics close to the heave resonance period lead to higher tensions in the mooring systems, whereas the maximum fluid-induced loads on the hull are decoupled from displacement peaks, showing an average reduction of 30% with respect to the maxima; very steep waves maximize the likelihood of wave overtopping and slamming loads, resulting in locally induced overpressure on the free-board of up to 100% higher than expected for similar wave heights with milder profiles. The input data for these last tests is released for the sake of reproduction.

1. Introduction

The dependency on electricity produced by offshore wind is expected to increase immensely (IEA, 2022), but there are still large knowledge gaps on their dynamics and performance in severe ocean conditions. In particular, this holds true for emerging floating offshore wind turbines (FOWT) technologies. FOWTs pose significant challenges due to their hardware assembly (Butterfield et al., 2007), working behavior at sea, (Fang et al., 2023), and overall environmental complexity (Rehman et al., 2023). Various substructure concepts have been proposed for offshore wind turbines (Myhr et al., 2014), including spar-like structures (Karimirad and Moan, 2012), tension-leg platforms (TLPs) (Oguz et al., 2018), and semi-submersible foundations (Jiang, 2021; Asim et al., 2022). Currently, semi-submersible platforms for horizontal axis wind turbines appear to be favored due to several technological advantages, including cost-effective construction, established mooring layouts (Chen and Yang, 2021), and reduced downtime in operational sea states. The stability of a semi-submersible floating platform (SFP) depends on various factors, such as its geometry, mass distribution, and hydrodynamic forces acting on the structure (Anon, 2009; Fowler et al., 2017). The size and shape of the pontoons and

* Corresponding author.
E-mail address: alexbexe@uvigo.es (A.J.C. Crespo).

https://doi.org/10.1016/j.apor.2023.103757
Received 15 May 2023; Received in revised form 3 October 2023; Accepted 4 October 2023
Available online 19 October 2023

columns, for example, can affect the stability of the platform in different sea states (Lopez-Pavon and Souto-Iglesias, 2015). Additionally, plates play an important role in the stability of SFPs by increasing their buoyancy and reducing their draft.

In recent years, the research area of *ocean hydrodynamics* has received increasing attention (Tavakoli et al., 2023). Numerical-wise, fluid dynamics is tackled using two main levels of modeling framed according to their level of fidelity, which therefore apply to FOWT simulations (Otter et al., 2022). *Low-fidelity* modeling applied to offshore structures involves creating quick and simple representations of the prototype using digital tools such as wireframe software and analytical models (Varghese et al., 2022). The goal of low-fidelity modeling is to quickly test and explore design ideas in the early stages of the design process to receive feedback and refine concepts. As the model progresses towards later stages of the design process, its complexity increases, and *high-fidelity* prototyping comes into play (Papalambros and Wilde, 2017). This process involves creating more polished and detailed prototypes that closely resemble the final product, often using advanced tools. High-fidelity prototypes aim to provide a highly accurate and realistic representation of the final product, allowing designers to develop more confidence in their design (Otter et al., 2022). Within numerical modeling, computational fluid dynamics (CFD) is recognized as the most advanced tool for directly investigating the fluid flow governing equations by solving them in time and spatial domains to obtain transient hydro- and aero-dynamic loading.

Mid-fidelity solutions can be conceived for predicting the response of FOWTs. One such solution is integrated into the software toolbox called OpenFAST (Open-source Fatigue, Aerodynamics, Structures, and Turbulence), developed by the National Renewable Energy Laboratory (NREL, US) to simulate the combined effects of wind and waves on wind turbines. The *limitations* of mid-fidelity modeling for offshore renewable energy devices is primarily based on its use of potential-flow theory for hydrodynamic analysis, solved using software such as HydroDyn (Jonkman, 2007), or similar linear solvers (OrcaFlex or REEF3D (Wang et al., 2022a; Bihs et al., 2020)). These kinds of method solve the Laplace equation for the velocity potential function, which describes fluid flow based on the distribution of sources, sinks, and vortices. However, this approach has limitations due to assumptions of inviscid fluids, the absence of turbulence modeling, constraints in boundary conditions, and complexities in modeling intricate geometries (see, e.g., Davidson et al., 2015; Davidson and Costello, 2020). Thus, the capabilities of the model in predicting loads in situations outside of relatively simple flow conditions are restricted (Kvittem et al., 2012). Mid-fidelity modeling limitations are mostly addressed by incorporating fictitious treatments for viscosity and other effects; these require case-specific model tuning. In certain scenarios, such as those related to survivability, mid-fidelity modeling capabilities are insufficient. Therefore, high-fidelity modeling is necessary to accurately predict loads and responses, as under extreme sea conditions, where second-order hydrodynamic effects can have larger impacts on the overall dynamic responses of SFP (Shi et al., 2023).

The importance of anticipating wave-induced loads on offshore structures under *severe* environmental conditions (as specified in DNV-ST-0119, 2016) cannot be overstated for their secure deployment (van Essen and Seyffert, 2023), and linear solvers may not be able to predict such load conditions. State-of-the-art CFD software can accurately predict wave impact loads, such as slamming (compare, experiments in Göteman et al., 2015 and numerical simulations in Katsidoniotaki and Göteman, 2022 or Tagliafierro et al., 2022d; Shahroozi et al., 2022 and Katsidoniotaki et al., 2023), which is highly relevant for reliably assessing ultimate limit state safety factors for offshore structures (see about application of CFD-based methods, Oger et al., 2014; Bandringa and Helder, 2018; Huang et al., 2022; Zeng et al., 2023a). As trivial as it may seem, a crucial step forward on the use of CFD, and therefore its applicability to renewable energy, has revolved around the simulation of wave energy converters (WECs) (Opoku et al., 2023). CFD successfully complemented the design process of WECs (Windt et al., 2018), leading to the development of adequate features within advanced CFD solvers, such as OpenFOAM (Sjökvist et al., 2017; Ransley et al., 2017; Katsidoniotaki and Göteman, 2022) or GPUSPH (Wei et al., 2019). However, the complex and multi-connected hardware nature of floating offshore wind turbines presents challenges in modeling them as manageable sub-systems due to two main reasons: the strong-coupled wind-wave induced response across system components, such as mooring (Yan et al., 2023) and servo control systems that can potentially modify in-time the system's response (Zhang et al., 2020; Roald et al., 2013). While CFD simulations have been shown to be very comprehensive and realistic, such as those in Liu et al. (2017) or Zhou et al. (2019), downgrading the complexity of the FOWT model remains difficult.

Several studies have highlighted potential issues with the use of potential-flow based solvers to estimate wave–structure interactions. For instance, Tran et al. (2014) conducted CFD simulations using the mesh-based solver CD-Adapco STAR-CCM+ on a floating offshore wind turbine (FOWT) subject to platform pitching motion and compared against FAST simulations. The researchers found that the pitch motion can significantly impact the turbine's aerodynamic performance. Specifically, the blade pitch angle and rotor rotational speed were affected by the platform pitching motion, which, in turn, influenced the power output of the turbine. A study by Nematbakhsh et al. (2015) compared the wave load effects on a TLP wind turbine using two methods: a mesh-based in-house CFD solver and potential flow theory. The study found that the latter method consistently overestimated the wave load effects on the TLP tendons, while the mesh-based one provided more accurate results. The authors concluded that CFD methods may be a more reliable and accurate approach to predicting wave load effects on TLP wind turbines than the potential flow theory method. Similarly, Oguz et al. (2018) experimentally simulated TLP coupled loads using software-in-the-loop (SIL)-based systems to represent blade aerodynamic loads and compared the results against the FAST simulator (HydroDyn). The authors found that the numerical solver overpredicted the maximum tendon tensions, which were attained during the maximum surge motion. More recently and comprehensively, systematic research carried out by the Offshore Code Comparison Collaboration Continued with Correlation (OC5 - Robertson et al. (2017)) highlighted the *persistent underprediction* of load and motion magnitudes by engineering tools used during the restitution phase. The research posits that the misrepresentation of low-frequency loads may stem from inaccurate fluid resolution (Robertson et al., 2020b). Consequently, the ensuing Offshore Code Comparison Collaboration, Continued with Correlation, and unCertainty (OC6) project aimed to assess the sources of inaccuracy and perform more focused investigations to improve the general credibility of CFD methods through validation (see, regarding OC projects results Wang et al., 2022c, 2021; Robertson and Wang, 2021).

In the field of CFD, the Navier–Stokes equations form the basis for solving fluid dynamics problems. Historically, these equations have been tackled adopting grid-based methods (Harlow, 2004), but in recent years, mesh-less methods have gained popularity (Liu and Liu, 2003; Violeau, 2012; Sriram and Ma, 2021). Among these, the Smoothed Particle Hydrodynamics (SPH) method (Monaghan et al., 1999; Gomez-Gesteira et al., 2012) is a particle-based technique that has shown promise for a wide range of engineering applications (Amicarelli et al., 2020), including offshore engineering (Gotoh and Khayyer, 2018) or fluid–structure interactions in ocean engineering (Gotoh et al., 2021). In fact, research efforts have been channeled towards the development of SPH-based solvers for modeling violent fluid dynamics, as the method's unique features make it well-suited for this task (Davidson and Costello, 2020). One of the main advantages of mesh-less methods such as SPH is that they overcome the mesh distortion issues that have been commonly encountered with grid-based solvers (as discussed in Rakhsha et al., 2021; Katsidoniotaki et al., 2023). This makes SPH an attractive option for simulating offshore structures, as it can accurately

model the complex flow phenomena that occur under severe environmental conditions. Although the application of mesh-free methods to support offshore engineering is growing at a fair pace (Luo et al., 2021), there is still a need to promote their use and increase their visibility (Violeau and Rogers, 2016). As noted in Tavakoli et al. (2023), further efforts are required to encourage the adoption of mesh-less methods such as SPH, in order to attract more research efforts in that direction.

The available literature provides a strong background on the usability of particle-based methods in simulating waves interacting with platforms that exhibit high degrees of mobility and frequency responses close to those relevant in the renewable energy sector, such as wind and solar. However, while these methods show promise for forthcoming practical applications, such as survivability investigations, knowledge and reliability gaps still persist regarding their usability and applicability. This is exemplified by the outcome of the OC6 Phase Ia study (Wang et al., 2022b). The study involved the collective effort of several institutions in simulating free-decay tests for the DeepCwind using CFD. Of the 11 participating partners, nine utilized the open-source OpenFOAM software in various versions, while the remaining partners used commercially available CFD-based software (such as STAR CCM+). These findings suggest a low level of penetration of particle-based methods in the industry.

Prior investigations on FOWTs using SPH have shown great potential, leveraging the advantages of mesh-less approaches such as easier implementation of coupling techniques (Masud and Hughes, 1997; Fries and Matthies, 2006). To the best of our knowledge, the following references represent the state of the art for using SPH-based models in FOWT simulations. Leble and Barakos (2016a,b) proposed a *demonstration* of the potential of the SPH method for SFPs under simultaneous wave and wind loads, using the SPH method for hydrodynamic modeling and a blade-resolved model for the turbine. The platform stability was ensured by a set of mooring lines. Although promising and constituting a vanguard solution, this model has not been further developed. Tagliafierro et al. (2022a) and Tagliafierro et al. (2022b) investigated the response of a TLP under regular and irregular waves, focusing on the effects of hydrodynamic non-linearity leading to a skewed force pattern in the mooring system. Wave and structure interactions were well-captured, overcoming the limitations of reduced-order models for large displacement. In Pribadi et al. (2023), an SPH reduced wave basin was developed for wave generation and propagation, set around the semi-submersible platform OC5-DeepCwind (Robertson et al., 2017). The mooring system included virtual catenary lines anchored well outside the extension of the water environment. Lastly, Tan et al. (2023) recently presented an SPH solver coupled to a lumped-mass simulator for mooring lines to investigate the NREL OC4-DeepCwind platform (Robertson et al., 2014). The model was validated against experimental data obtained with a ≈1/210-scaled model under regular and irregular waves. The SPH predictions showed good accuracy in solving the motion of the moored FOWT model under multiple regular wave conditions.

After conducting a state-of-the-art review, the use of a numerical simulator based on the SPH method called DualSPHysics (Domínguez et al., 2022) has been considered. DualSPHysics is open-source software that is distributed under an LGP license, which is aimed at promoting SPH research and development. The software has been widely used in various research areas, including coastal engineering (Altomare et al., 2022; Mitsui et al., 2023; Pringgana et al., 2023). For our research, we specifically used the version of DualSPHysics coupled with the multiphysics library Project Chrono (Tasora et al., 2016) that was presented in Martínez-Estévez et al. (2023a). DualSPHysics has been extensively used to simulate offshore renewable energy, particularly a variety of WEC concepts (point absorbers (Ropero-Giralda et al., 2020; Tagliafierro et al., 2022d), oscillating water columns (Crespo et al., 2017; Quartier et al., 2021), and oscillating wave surge converters (Brito et al., 2020; Tagliafierro et al., 2022c)). It is worth mentioning that almost all the recent research using SPH applied to FOWTs has been performed using DualSPHysics respectively, Tagliafierro et al. (2022b,a), Pribadi et al. (2023), and Tan et al. (2023), with an earlier version of the code being coupled with MoorDyn+ (Domínguez et al., 2019b).

Our research stands as the first systematic validation of the SPH technique using the well-established benchmark of the semi-submersible platform DeepCwind for FOWTs. This validation encompasses a wide range of wave-induced loads generated by different wave models. We rigorously validate these loads by comparing time history responses and spectral analyses on a fully resolved structure. Furthermore, we conduct dynamic validation of the system during free decay tests, employing the same floater configuration without any kinematic restrictions other than the mooring lines. After this preparatory work, a thorough investigation into the response of the DeepCwind platform under extreme events for which the hydrodynamics is investigated in detail, capturing the evolving local pressure and turbulent fields. After an initial literature survey, the paper provides the numerical method in Section 2, focusing on the fluid phase resolution and the mooring system handler. In Section 3, we introduce the experimental data setups and translate them into the numerical geometries for subsequent simulations. We present comparisons for the free-decay motion and hydrodynamic loads in Section 4, and investigate wave-induced hydrodynamic loads induced by focused waves in Section 5, encompassing local and global quantities. Finally, we draw conclusions from our work and outline future research prospects in Section 6.

2. The SPH model

This section describes the main formulation and the governing equations of the SPH method that are implemented in the DualSPHysics code version 5.2 (https://dual.sphysics.org/downloads/) (Domínguez et al., 2022), along with the equations to solve the rigid body dynamics of the fluid-driven objects, the approaches available for wave generation and propagation, and finally, the coupling procedure with the multiphysics library Project Chrono to solve the fluid-solid interaction and the multi-body dynamics.

2.1. SPH basis

SPH is a Lagrangian mesh-less method that discretizes a continuum into discrete particles, in which the motion is computed by interpolating the quantities of the neighbor particles. The set of neighbor particles and their contribution is obtained by a weighting function (W) (the so-called kernel), whose area of influence, Ω, is defined with a smoothing length (h). Thus, the SPH method is mathematically described as a convolution integral approximation of any function $F(\boldsymbol{r})$ following:

$$F(\boldsymbol{r}) = \int_{\Omega} F(\boldsymbol{r}')W(\boldsymbol{r}-\boldsymbol{r}')\mathrm{d}\boldsymbol{r}', \tag{1}$$

where $\boldsymbol{r}$ is the position of the target point and $\boldsymbol{r}'$ is the position of another point. The function F is approximated by interpolating the contribution of the neighbor particles in discrete form:

$$F(\boldsymbol{r_a}) = \sum_b F(\boldsymbol{r_b})W(\boldsymbol{r_a}-\boldsymbol{r_b}, h)\frac{m_b}{\rho_b}, \tag{2}$$

where subscripts a and b represent the target and the neighbor particles, respectively, h is the smoothing length, m is the mass, and ρ is the density. In addition, the kernel function $W(\boldsymbol{r}, h)$ employed in this work is the quintic Wendland kernel (Wendland, 1995), defined as:

$$W(q) = \alpha_D \left(1-\frac{q}{2}\right)^4 (2q+1), \quad \text{with } 0 \le q \le 2 \tag{3}$$

where α_D is a real number set to $21/16\pi h^3$ in 3D, $q = r/h$ is the non-dimensional distance between particles, and r is the distance between particles a and b.

2.2. Governing equations

The Navier–Stokes equations are the governing equations in fluid dynamics. In the SPH method, the Navier–Stokes equations are employed to dictate the dynamics of the particles. Then, in Lagrangian form, momentum and continuity equations can be discretized, respectively, as:

$$\frac{\mathrm{d}\boldsymbol{v_a}}{dt} = -\sum_b m_b \left(\frac{p_a + p_b}{\rho_a \rho_b}\right) \nabla_a W_{ab} + \boldsymbol{\Gamma}_a + \boldsymbol{g}, \tag{4}$$

$$\frac{\mathrm{d}\rho_a}{dt} = \rho_a \sum_b \frac{m_b}{\rho_b} \boldsymbol{v}_{ab} \cdot \nabla_a W_{ab} + D_a, \tag{5}$$

being the operator definition $(\cdot)_{ab} = (\cdot)_a - (\cdot)_b$, W_{ab} is the kernel function, t is the time, $\boldsymbol{v}$ is the velocity, p is the pressure, and $\boldsymbol{g}$ is gravitational acceleration constant. The term $\boldsymbol{\Gamma_a}$ in Eq. (4) introduces dissipation as described by:

$$\boldsymbol{\Gamma}_a = \sum_b m_b \frac{4\upsilon_0 \boldsymbol{r}_{ab} \cdot \boldsymbol{\nabla}_a W_{ab}}{(\rho_a + \rho_b)\left(r_{ab}^2 + 0.01h^2\right)} \boldsymbol{v}_{ab} + \sum_b m_b \left(\frac{\tilde{\tau}_a^{ij} + \tilde{\tau}_b^{ij}}{\rho_a \rho_b}\right) \nabla^i W_{ab}. \tag{6}$$

The first term on the right-hand side of Eq. (6) introduces the so-called laminar viscosity (Lo and Shao, 2002), where the term $\upsilon_0 = 1.0 \times 10^{-6} \mathrm{m}^2/\mathrm{s}$ refers to the kinematic viscosity of the fluid.

The second term describes the sub-particle scale model (SPS) (Dalrymple and Rogers, 2006), corresponding to the variationally consistent form of the symmetric formulation proposed in Lo and Shao (2002). The SPS stress tensor, $\tilde{\tau}^{ij}$, in Einstein notation in coordinate directions i and j, is defined according to SPS strain tensor:

$$\tilde{S}^{ij} = -\frac{1}{2}\left(\frac{\partial \tilde{v}_i}{\partial x_j} + \frac{\partial \tilde{v}_j}{\partial x_i}\right), \tag{7}$$

where $\mathbf{x}$ is the position of the particle. Its formulation is modeled via Eddy viscosity assumptions, using the standard Smagorinsky model:

$$\frac{\tilde{\tau}^{ij}}{\rho} = \nu_t \left(2\tilde{S}^{ii} - \frac{2}{3}\tilde{S}^{ii}\delta^{ij}\right) - \frac{2}{3} C_L \Delta^2 \delta^{ij} |\tilde{S}^{ij}|^2. \tag{8}$$

In Eq. (8), $\nu_t = \left(C_S \Delta\right)^2 |\tilde{S}^{ij}|$ is the eddy viscosity, $C_S = 0.12$ the Smagorinsky constant (Smagorinsky, 1963), $C_L = 0.0066$ as per (Blin et al., 2003), whereas Δ represents the initial particle spacing; $|\tilde{S}^{ij}| = \frac{1}{2}\left(\tilde{S}^{ij}\tilde{S}^{ij}\right)^{1/2}$ is, indeed, the local strain rate, and δ^{ij} is the Kronecker delta function.

A density diffusion term (D) is included to Eq. (5) to reduce fluctuations in the density, following Fourtakas et al. (2019), that is expressed as:

$$D_a = 2\delta h\, c_s \sum_b (\rho_{ba}^T - \rho_{ab}^H) \frac{\boldsymbol{r}_{ab} \cdot \nabla_a W_{ab}}{r_{ab}^2} \frac{m_b}{\rho_b}, \tag{9}$$

where c_s is the speed of sound, $\delta = 0.10$ is the coefficient that controls the diffusive term, and superscripts T and H are the total and hydrostatic components of the density, respectively, that characterizes weakly compressible fluids. The hydrostatic pressure is computed as:

$$\rho_{ab}^H = \rho_0 g z_{ab}, \tag{10}$$

where z_{ab} position difference in z between particles a and b.

This approach for the density treatment is based on the formulation proposed by Molteni and Colagrossi (2009), which leads to some inconsistencies near the wall boundaries (Fourtakas et al., 2019). However, in Fourtakas et al. (2019), a correction has been introduced to replace the total dynamic density with the dynamic density and so, the behavior of pressure near the wall boundaries becomes consistent with the pattern exhibited by the surrounding fluid particles. As opposed to the delta-SPH formulation proposed by Antuono et al. (2012), the approach eliminates the need for computing the normalized density gradient, which reduces the computational cost. Although the delta-SPH has more general applicability to a variety of physics, the formulation employed in this work can be accurately applied to solve gravity-dominated flows (Fourtakas et al., 2019).

Since DualSPHysics implements a weakly compressible SPH formulation to solve the fluid, then an equation of state is used to compute the fluid pressure (p) from the density (ρ),

$$p = \frac{c_s^2 \rho_0}{\gamma_p}\left[\left(\frac{\rho}{\rho_0}\right)^{\gamma_p} - 1\right], \tag{11}$$

where ρ_0 is the reference density of the fluid and $\gamma_p = 7$ is the polytropic constant.

The implementation is completed via the time integrator scheme known as Symplectic (symplectic position Verlet) (Leimkuhler et al., 1995), which is an explicit and second-order accurate in time. Additionally, a variable time step is used to enforce the Courant-Friedrich-Lewy (CFL) condition, in which the force and the viscous diffusion terms follow the implementation in Monaghan and Kos (1999). Details on the implementation of the time integrator scheme and the variable time step in DualSPHysics, as well as on the governing equations, are given in Domínguez et al. (2022).

The boundary conditions (BCs) are implemented according to the formulation presented in English et al. (2022), so-called mDBCs (modified DBC). This approach overcomes minor inconsistencies of previous implementations, such as large gaps between fluid and boundary particles appearing when transition from non-wet to wet takes place. The particle layout for mDBC requires extra information to compute the solid-fluid interaction, making use of a boundary interface to locate the transition layer between the BCs and the fluid domain. This surface is used to enforce a mirroring technique utilizing ghost nodes from the boundary particles into the fluid domain. On those fictitious node positions the fluid properties are evaluated; the SPH computation thus leverages those values to consistently interpolate the solid particles quantities (Liu and Liu, 2006). The use of mDBC can guarantee precise pressure computation, as shown in English et al. (2022), Capasso et al. (2021), and reduces the non-physical gap between boundary and fluid particles (Altomare et al., 2021; Suzuki et al., 2022).

2.3. Rigid body dynamics

DualSPHysics implements the equations of rigid body dynamics to simulate the motion of fluid-driven objects, which are solved as rigid bodies governed by the Navier–Stokes equations. Then, assuming that a rigid body is discredited as set of boundary particles, each boundary particle k experiences a force per unit mass ($\boldsymbol{f}_k$) obtained from the acceleration ($\mathrm{d}\boldsymbol{v}/\mathrm{d}t$), given by:

$$\boldsymbol{f}_k = \sum_b \frac{\mathrm{d}\boldsymbol{v}_{kb}}{\mathrm{d}t} + \boldsymbol{g}. \tag{12}$$

Then the basic equations of rigid body dynamics are solved to obtain its motion as:

$$M\frac{\mathrm{d}\boldsymbol{V}}{\mathrm{d}t} = \sum_k m_k \boldsymbol{f}_k, \tag{13}$$

$$I\frac{\mathrm{d}\boldsymbol{\Omega}}{\mathrm{d}t} = \sum_k m_k \left(\boldsymbol{r}_k - \boldsymbol{R}_0\right) \times \boldsymbol{f}_k, \tag{14}$$

where M is the total mass of the object, I the moment of inertia matrix, $\boldsymbol{V}$ the velocity, $\boldsymbol{\Omega}$ the angular velocity and $\boldsymbol{R}_0$ the center of mass. Then, Eqs. (13) and (14) are integrated in time to obtain the values of $\boldsymbol{V}$ and $\boldsymbol{\Omega}$ at the beginning of the next time step. Each boundary particle belonging to the body has the following velocity:

$$\boldsymbol{v}_k = \boldsymbol{V} + \boldsymbol{\Omega} \times \left(\boldsymbol{r}_k - \boldsymbol{R}_0\right). \tag{15}$$

This technique has been further discussed by Monaghan et al. (2003), where it has been proven that it ensures the conservation of linear and angular momentum. Validations with DualSPHysics can be found in Canelas et al. (2015) or Domínguez et al. (2019b).

2.4. Wave generation and propagation

The DualSPHysics code has been developed to pursue applicability towards the simulation of coastal protections and offshore structures. As a result, the code implements several tools, based on different techniques for coastal-related problems, to generate sea waves with various techniques so as to have a wide choice of methods to be deployed for specific case requirements. In particular:

- **moving boundary particles**: much like physical wave flumes and basins, this technique, common to many other software distributions, utilizes the displacement of piston- or flap-type wavemakers according to 1st and 2nd order wave theory-generated solution for regular and random waves (Altomare et al., 2017) or solitary waves (Domínguez et al., 2019a);
- **relaxation zones**: employed either as a stand-alone generation method or as a coupling method with other phase-resolving models (Altomare et al., 2018);
- **multi-layered piston wavemaker**: the multi-layer piston consists of a set of boundary particles that move as a whole rigid body (Altomare et al., 2015); and
- **open boundaries**: well suited for two-way coupling with wave propagation models but also effective for stand-alone wave generation (Verbrugghe et al., 2019).

In this work, moving boundary particles are utilized to generate suitable free-surface elevation time series that possess properties as close as possible to the ones reproduced experimentally.

2.5. Coupling with project chrono

DualSPHysics is coupled to the multiphysics library Chrono (Tasora et al., 2016) to enhance its versatility. The coupling technique works as follows: the SPH method solves the fluid–solid interaction while Chrono solves the solid–solid interaction as it has been presented in Martínez-Estévez et al. (2023a). Then, the dynamics of the multibody systems composed by rigid bodies is computed, following (Tasora et al., 2016), as:

$$\frac{d\boldsymbol{q}}{dt} = \boldsymbol{L}(\boldsymbol{q})\,\boldsymbol{v}, \tag{16}$$

$$\boldsymbol{M}\frac{d\boldsymbol{v}}{dt} = \boldsymbol{F}_t(t,\boldsymbol{q},\boldsymbol{v}), \tag{17}$$

$$\boldsymbol{F}_t(t,\boldsymbol{q},\boldsymbol{v}) = \boldsymbol{F}_e - \boldsymbol{F}_c, \tag{18}$$

where $\boldsymbol{F}_e = \boldsymbol{F}_e(t,\boldsymbol{q},\boldsymbol{v})$ and $\boldsymbol{F}_c = \boldsymbol{F}_c(t,\boldsymbol{q})$. $\boldsymbol{L}(\boldsymbol{q})$ is a linear transformation of the generalized positions ($\boldsymbol{q}$), $\boldsymbol{v}$ are velocities, $\boldsymbol{M}$ is the total mass matrix, $\boldsymbol{F}_t$ is the total force, which is computed from the external ($\boldsymbol{F}_e$) and constraint forces ($\boldsymbol{F}_c$), respectively. In this work $\boldsymbol{F}_e$ is the force exerted by the fluid due to the fluid-solid interaction using the SPH method while $\boldsymbol{F}_c$ corresponds to multibody systems with mechanical constraints that restrict the motion of the rigid objects.

The degrees of freedom between rigid instances can include reactive forces according to their relative displacement. An element that is capable of exerting a similar force pattern ($\boldsymbol{F}_c$ in Eq. (18)) is called *spring-damper* element. The magnitude of the spring-damper force between two bodies i and j can be written as a linear superposition of a viscous and a spring term,

$$F_c = c_{sd}\boldsymbol{v}_{ij}\cdot\hat{\boldsymbol{t}}_{sd} + k_{sp}\boldsymbol{r}_{ij}\cdot\hat{\boldsymbol{t}}_{sd}, \tag{19}$$

where c_{sd} and k_{sd} are the viscous damping coefficient and spring stiffness that are implemented via the element, respectively; $\boldsymbol{r}_{ij}$ and $\boldsymbol{v}_{ij}$ are the relative position and velocity between points i and j. The term,

$$\hat{\boldsymbol{t}}_{sd} = \frac{\boldsymbol{r}_j - \boldsymbol{r}_i}{|\boldsymbol{r}_j - \boldsymbol{r}_i|}, \tag{20}$$

represents the direction along which the force is applied; $\boldsymbol{r}_i$ and $\boldsymbol{r}_j$ identify the position of the points i and j. Within the scope of this research, the mooring system of the floating structure is composed of spring-like cables, and can be described using Eq. (19). More information on the way the elements are detailed into the simulations are presented when the setup is discussed.

3. Case study

3.1. Experimental setup

For the numerical validation procedure that follows, the 1:50-scale DeepCwind semi-submersible is considered as a reference structure (Robertson et al., 2017). Data from two experimental investigations is used, which can be respectively found in Robertson et al. (2020b) and Robertson and Wang (2021). Fig. 1 proposes two pictures that were taken during OC6-PhaseIa (Fig. 1(a)) and OC6-PhaseIb (Fig. 1(b)).

The first experimental data collection considered here is related to *OC6-PhaseIa - sub- structure* (collected in Robertson et al., 2020b) and the measurements were proposed for the validation of engineering tools (low-fidelity). The tests were carried out at the Concept Basin of the Maritime Research Institute Netherlands (MARIN) (The Netherlands), and two load cases are considered in the following: calm-water free-decay motions in surge and heave. For our research, we employ the dataset available at A2e Data Archive and Portal for the DualSPHysics code validation in the same fashion of what is presented in Wang et al. (2021).

The testing campaign in Robertson and Wang (2021) (*OC6-PhaseIb - FOW substructural components*) was carried out at the W2 Harold Alfond Ocean Engineering Laboratory (University of Maine, US), pursuing the hydrodynamic loading pattern recognition on FOWT substructures. Due to its focus on low-frequency contributions, long-crested surface waves were generated by a flap-type wavemaker with 16 paddles in a 30 × 9 × 5 m basin, propagating lengthwise. An elliptical beach at the end of the basin was used to reduce wave reflection. The basin setup and instrumentation is reported with much more details in Dagher et al. (2017). During OC6-PhaseIb, as mentioned in the introduction, wave frequency-induced loads with close match to the semi-submersible dynamic properties were investigated, based on the observations reported in Robertson et al. (2020b). With that in mind, the investigated frequency band spans the spectrum around 0.50 Hz, with wave parameters that were able to trigger second-order wave interaction (see also, Fowler et al., 2017). Three main wave representations were used: regular, bi-chromatic, and irregular waves. Data employed during our validation work was downloaded from the database A2e Data Archive and Portal.

3.2. Numerical configuration

General setting

The model initialization, as for any CFD setup, represents an important step as the accuracy of the model prediction hinges on that. For the definition of the SPH geometrical configuration, having to deal with two different setups, details are given in two dedicated subsections, whereas here the common properties are described. In Figs. 2 and 3, the two test rigs are shown to reflect the differences in the way the decay and wave-loading tests are respectively performed. Shared by both, the fluid phase aims to mimic fresh water (complying with the physic parameters) using an initial phase density $\rho_0 = 998.6$ kg/m^3 (from experimental data), with speed of sound of $c_s = 150$ m/s, ensuring Ma < 0.10. The initial particle setup is created in DualSPHysics using a cubic lattice where particles are initially created at a constant initial inter-particle distance (dp). In fact, the smoothing length h is also defined in DualSPHysics as a function of dp. In this work we used $h = 2dp$,

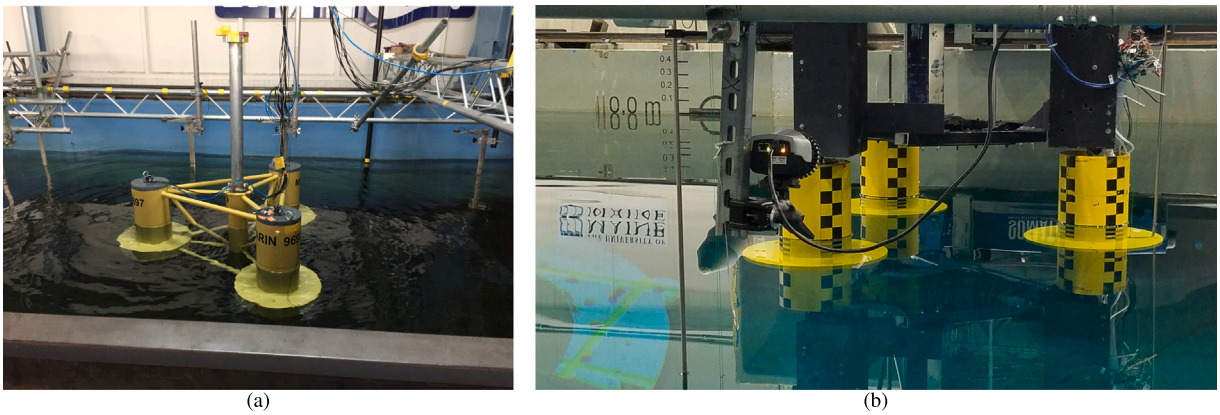

Fig. 1. Pictures of the models of the semi-submersible floating wind substructure investigated in this study. 1(a) The DeepCwind platform used in OC6-Phase Ia investigation; 1(b) The simplified floater geometry tested during OC6-Phase Ib (courtesy of Amy Robertson, NREL).

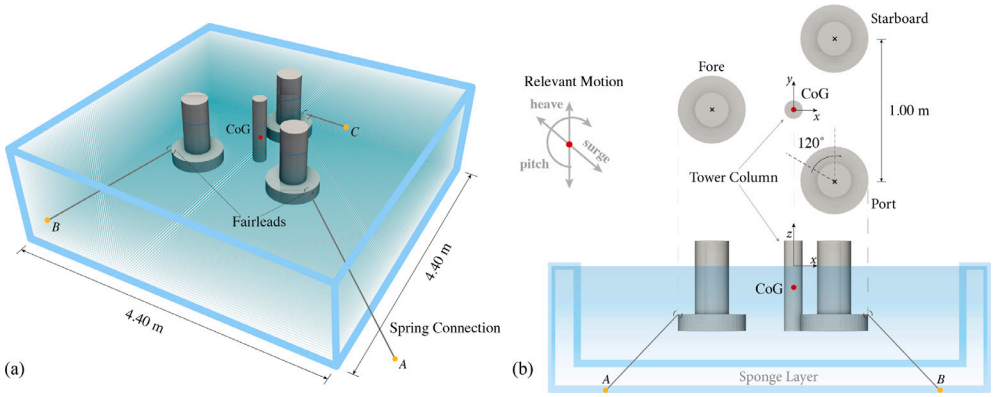

Fig. 2. Numerical setup for the free-decay testing of the DeepCwind floating offshore platform: (a) 3-D view, (b) side and top views.

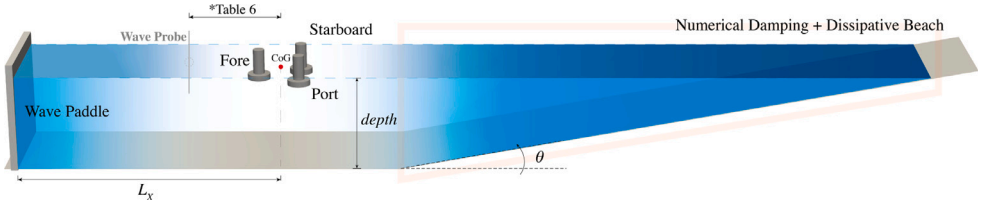

Fig. 3. The layout for the DeepCwind floating offshore platform for testing under wave loads.

so that the kernel interaction distance is $2h = 4dp$. The initial inter-particle distance, dp, is initialized targeting sensitivity analysis tests to be performed next, hence dp is defined with inverse proportionality to the plate thickness (P_T). Note that all the boundary particles are defined using the mDBC strategy (English et al., 2022) and briefly described in Section 2.

For both sub-phases, and regardless of the investigation objectives, the floater archetype used had been the OC4-DeepCwind semi-submersible (Robertson et al., 2014). As mentioned in the introduction, this platform is designed to support a single horizontal axis wind turbine and comprises three pontoons that are equally spaced in a three-pointed star configuration in its fully-fledged shape. However, in the tested layouts used for this validation, slight differences are observed when generating the representation of the full platform. The shape of the single pontoon remains the same across all the tests. Fig. 4 shows the basic assembly of cylinders and plates that characterize the hydrodynamic interaction of the platform with ocean waves, with the main dimensions tagged. Additionally, Fig. 4 shows the location of the pressure sensors (UF4 and BF4) and the run-up sensor, which are arranged according to the spatial coordinates given in Table 1, with respect to a local system of reference.

Table 1
Position of the pressure gauges in the local system of the column.

ID	x' [m]	y' [m]	z' [m]
UF4	−0.120	0.000	0.385
BF4	−0.225	0.000	0.120
Runup Conf. D	−0.141	0.000	0.400
Runup Conf. P	−0.136	0.000	0.400
Runup Conf. Q[a]	−0.136	0.000	0.400

[a] Note that the vertical probe is rotated according to the column pitch when specified.

Decay test configuration for OC6-PhaseIa

To perform numerical free-decay surge and heave tests, the water tank shown in Fig. 2 is employed. The geometry of the float reflects the configuration setup realized in the experimental campaign of Robertson et al. (2020b), with little adjustments that aim to reduce the complexity

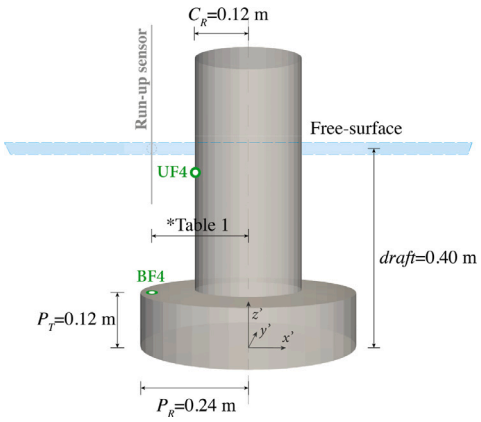

Fig. 4. Detailed view of the single pontoon with the 12-cm plate.

Table 2
Model scale dynamic properties of the DeepCwind platform.

Description	Symbol	Value
Displaced Volume	V_P [m^3]	0.106
Center of Buoyancy	CoB_z [m]	−0.263
Center of Gravity	CoG_z [m]	−0.151
Mass	M_P [kg]	96
Roll Moment of Inertia	I_{xx} [kg m^2]	40
Pitch Moment of Inertia	I_{yy} [kg m^2]	40
Yaw Moment of Inertia	I_{zz} [kg m^2]	44

of the platform assembly owing to the geometrical limitations in the current SPH framework. The platform comprises three pontoons, each of which preserves the geometry depicted in Fig. 4, and a central column that idealizes the support for the turbine tower. However, the bracing system that connects the four mentioned volumes that are also visible in Fig. 2(b) are not embedded within the SPH discretization due to their smaller size in comparison to other elements that are involved in the simulation. This is important to frame some of the discrepancies that will be visualized in the comparison in the following section. Nevertheless, the three floaters and the central column behave as a sole rigid body by embedding them within a shared rigid frame.

The properties that are required to model the platform in a dynamic system are given in Table 2. They refer to a simplified version of the OC5-DeepCwind FOWT (Robertson et al., 2014), in which a rigid tower and block mass were used to proxy the presence of a horizontal axis rotor-nacelle wind turbine installed on top of the float. Note that the displaced volume (V_P) refers to the structure with platform draft equal to the one of the single pontoons and only accounts for the simulated geometry (i.e., no bracings), whereas the mass is computed using Froude scaling. Due to the fact that the buoyancy will not reach the experimental one owing to the models' lack of consistency, the mass is set such that it balances the buoyancy force and the tendon forces. As for the mass moment of inertia, the factor correction discussed in Appendix A is applied to the experimental values fully, as no further information is available on the mass distribution.

The platform has six degrees of freedom (DOFs), and its motion is subject to the elastic forces provided by a system of taut-lines (see Fig. 2(a) and (b)). The mooring system comprises soft-spring lines that were intended to provide the same stiffness of the original catenary configuration OC4-DeepCwind, but restricted within a linear range to reduce the level of uncertainties of the system response (Robertson et al., 2020a). The line properties are reported in Table 3, whereas Table 4 proposes the positioning of the anchoring points and the fairlead locations according to a frame of reference located at the CoG of the platform in x and y, and z corresponds to the free surface in still water. The unstretched length and the initial pretension that are used to initialize the springs correspond to the scaled reference values. For this

Table 3
Mooring line kinematic and dynamic properties used for the initialization of the spring-damper elements.

Description	Symbol	Value
Cross-sectional stiffness	EA_l [N]	24
Nominal diameter	D_N [mm]	3.0
Line stiffness	K_l [N/m]	21.68
Line density	ρ [kg/m^3]	2000
Distributed mass	ρ_l [kg/m]	0.070
Unstretched length	L_0 [m]	1.11
Pretension	T_{ini} [N]	10.5

Table 4
Geometry of the mooring lines at equilibrium.

ID	Description	Connection	x [m]	y [m]	z [m]
A	Fore	Fairlead	−0.82	0.00	−0.28
		Anchor	−2.11	0.000	−1.08
B	Starboard	Fairlead	0.41	0.71	−0.28
		Anchor	1.05	1.83	−1.08
C	Port	Fairlead	0.41	−0.71	−0.28
		Anchor	1.05	−1.83	−1.08

Table 5
Tested configuration for wave hydrodynamics.

ID	Assembly	P_T [m]	Draft [m]	Pitch [deg]
Configuration D	1 Cyl. + 1 Plate	0.12	0.40	0
Configuration P	3 Cyl. + 3 Plates	0.12	0.40	0
Configuration Q	3 Cyl. + 3 Plates	0.12	0.40	5.0

Table 6
Position of the Wave Probe given as distance from the CoG of the model location (red dot in Fig. 3).

Configuration	x [m]	y [m]	z [m]
D	−2.48	−0.40	–
P	−2.50	−1.20	–
Q	−2.50	−1.20	–

research, due to the special configuration for the mooring lines, which are set up so that they are always engaged in tension, the mooring lines are represented by virtual spring-damper elements, as described by Eq. (19). Their competing mass is lumped and assigned to the overall platform mass (M_P in Table 2).

Wave basin configuration for OC6-PhaseIb

For the physical testing performed under the OC6-PhaseIb, the wave-induced hydrodynamic loads were measured on a fixed hull comprising different hull configurations. Three columns were independently mounted to a fixed frame from above, allowing for the introduction of a six DOF load cell in between the ground and the structure. We consider the three hull configurations reported in Table 5. Configuration D comprises only one of the base elements depicted in Fig. 4, whereas Configurations P and Q have three separate hulls shaped according to Fig. 4. As shown in Fig. 3, the three floaters are equally spaced by their symmetry axis by 1.00 m. The simplified floater geometry without the central main column and the cross-members used in OC6 Phase Ib was designed such that it avoids undesired interaction and disturbances from other components, thus isolating wave interaction and transformation with the structure.

The DualSPHysics platform provides a wide set of built-in functions that can be used to design suitable numerical tanks that are capable of generating the same wave profiles with overall relaxed dimensions when compared to the physical ones. A schematic representation of the numerical tank is presented in Fig. 3, in which a perspective view of the basin is sketched. On the left-hand side, the numerical tank features a piston-type wavemaker equipped, with an active wave absorption system (AWAS) (for regular and irregular waves) that actively supervise

Table 7
Description of the wave conditions. The numerical water depth is set to 2.00 m.

ID	Description	Wave height [m]	Period [s]	Depth [m]	Wavelength [m]	Simulated time [T]
R1	Regular (1)	0.146	1.67	2.00	4.32	Conf. D, P, Q = 20
R2	Regular (2)	0.068	1.67	2.00	4.32	Conf. D, P, Q = 20
B1	Bi-chromatic	0.069, 0.070	1.22, 1.68	2.00	–	Conf. D, P, Q = 50
J1	JONSWAP	0.138	1.68	2.00	4.32	D = 1000 P = 500 Q = 500

the quality of the generated waves on account of disturbances that the platform may launch towards the piston (see, Altomare et al., 2017). The width of the tank is set to three times the apparent size of platform (4.40 m) (three times the diameter of the plate for Configuration D), and this has proved sufficient to avoid any self-exiting water displacement. The lateral surfaces of the basin are created by the use of periodic boundary conditions that in principle create a contact layer between the back and the front of the flume (see, Gomez-Gesteira et al., 2012). On the right-hand side, an anti-reflective beach features a slope of $\theta = \pi/4$ rad, with an additional numerical damping; their combination efficiently absorbs the incoming waves, preventing any significant wave reflection (as a matter of fact, the numerical reflection coefficient thus obtained falls within 3%, depending on the wave conditions). The wave flume is instrumented with a wave probe that is located upstream of the model position, as specified in Table 6. The length-wise distance complies with the experimental specification for the capacitive wave probe labeled B (Robertson and Wang, 2021), whereas the cross wave-wise distance is assumed shorter to comply with the reduced size of the tank width.

The waves generated and propagated in the present basin are listed in Table 7; for each of them, a synthetic description of the crucial parameters are reported. Note that the ID in the first column is consistent with the nomenclature proposed by the referred database categorization. To guarantee the correct input incident wave reaching the platform, the center of gravity of the OC6 platform is placed at a distance indicated with L_X from the paddle, which is chosen as slightly bigger than the wavelength (L) of the incoming wave. The flume length, hence, is defined as $\propto L$, which can be obtained through the dispersion formula that relates the wave period and the water depth over which the wave is traveling. Note that the last column of Table 7 reports information regarding the simulated time (as multiple of the wave period) per each wave configuration with respect to the floater configuration. Longer simulations were run for Configuration D (sole column configuration) due to its relative lower computational cost.

The numerical wave elevation and runup are determined using a consistent approach. We define a set of points forming a numerical probe that in general forms a vertical line, but it can be however inclined. At each of these points, the mass is computed through the SPH approximation, taking into account the mass of surrounding fluid particles. Consequently, the free surface elevation is identified at the point of the numerical probe where its mass value reaches half of the reference mass (equivalent to the mass of a fluid particle).

Second-order wave generation with piston paddle

The wave conditions R1 and R2 in Table 7 are well described by second-order Stokes', which are basically the result of a superposition of two linear waves with different wave height, frequency, and phase. They have temporal consistent periods and wave heights, and there is not much wave transformation expected as they travel over a flat bathymetry. As introduced in Section 2.4, the piston-type wavemaker motion is able to generate first and second order regular waves according to the Stokes' theory (Dean and Dalrymple, 1984). The free-surface elevation for the latter is given by:

$$\eta = \frac{H}{2}\cos(kx - \omega t + \phi) - \\ - k\frac{H^2}{4}\frac{3-c^2}{4c^3}\cos(2(kx - \omega t + \phi)), \tag{21}$$

where H is the wave height, $k = 2\pi/L$ is the wavenumber, $\omega = 2\pi/T$ is the angular frequency, ϕ is the phase angle, $c = \tanh kd$, x and t are position and time, respectively. Nevertheless, DualSPHysics implements second-order wavemaker theory based on the correction developed by Madsen (1971) that has been demonstrated to prevent the generation of spurious waves. The details regarding the implementation in DualSPHysics are given in Altomare et al. (2017).

The wave condition B1 in Table 7 is a bi-chromatic wave train composed of two components that differ in frequency. Numerical simulations of bi-chromatic waves can be used to study the interaction between waves of different frequencies or amplitudes, as well as the effects of wave breaking and turbulence, thus investigating the occurrence of non-linear interactions between waves and fixed or mobile structures. As the two components can be combined in a very huge variety of modes, for the purpose of our validation, the data about the B1 experimental dataset has been used to rebuild the piston motion to reproduce exactly the same time evolution of the free surface. This is done by reversing the transfer function procedure from information of a probe location, and knowing the distance from the generating source. The paddle motion can be therefore used to produce very accurately the same free surface as it will be shown later in the validation section.

Irregular wave representation

Lastly, the wave condition J1 in Table 7 is a spectrum-compatible wave series whose generation procedure is explained in the following. For this representation, it is necessary to use the definition of the time evolution of the sea state, defined by assuming the significant wave height (H_{m0}), and assigning a wave frequency spectrum (S_ω); both define two constraints for the definition of the surface profile evolution. The shape S_ω is based, according to the reference case, by the Joint North Sea Wave Observation Project (JONSWAP) wave power spectrum definition (Hasselmann et al., 1973), as:

$$S_{JP}(\omega) = \frac{\alpha g^2}{\omega^5}\exp\left[-\frac{5}{4}\left(\frac{\omega_p}{\omega}\right)^4\right]\gamma^{\exp\left[-\frac{(\omega-\omega_p)^2}{2\sigma^2\omega_p^2}\right]}, \tag{22}$$

where $\omega_p = 2\pi/T_p$ is the spectral peak angular frequency, α is the generalized Phillips' constant, γ is peak enhancement factor (here $\gamma = 3.30$), σ is the spectral width parameter that is 0.07 for $\omega_p \geq \omega$ and 0.09 for $\omega_p < \omega$. The surface elevation is then reconstructed using second order theory, including both long-crested waves and super-harmonic components. Further details on the theoretical and software implementation are given in Altomare et al. (2017, 2018).

In practice, the free surface of irregular sea states is defined as a combination of harmonics that are characterized by different phases. Those phases are pseudo-randomly selected from statistical distributions to ensure sufficient significance to the resulting wave as a random process. Owing to the absence of the phase information in the reference dataset, the free surface has only been constrained to be spectrum compatible, and as such, an experimental–numerical comparison will be enforced in spectral terms.

Focus wave representation

In the conclusive phase of this research, and after the validation stage, unidirectional crest-focused waves are used to complement this study with the SPH method. Focused waves are defined according to the *NewWave* theory (Whittaker et al., 2017), although other theories have been developed so far (e.g., Gaussian wave packet by Clauss and

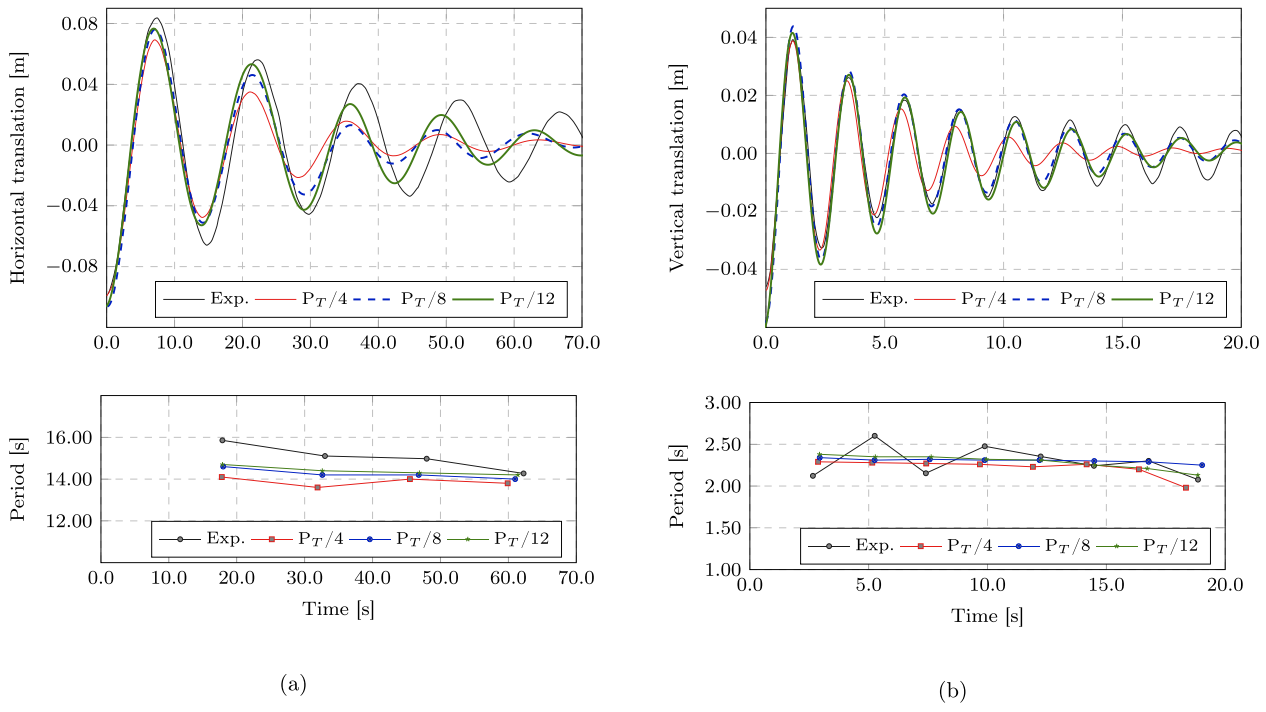

Fig. 5. Free-decay motion of the floater in (a) surge and (b) heave. In the first row, the time evolution for the two tests are shown, whereas the second row proposes the experimental and numerical zero-upcrossing periods in time.

Bergmann, 1986). Tromans et al. (1991) proposed the NewWave linear theory through the definition of the free-surface elevation $\eta(x,t)$ as linear superposition of N wave modes with respect to a sea-state power density spectrum $S_{(\omega)}$. Crest-focused wave groups are defined as:

$$\eta(x,t) = \sum_{n=0}^{N} a_n \cos(k_n(x - x_f) - \omega_n(t - t_f)), \tag{23}$$

where x_f and t_f are the focusing position and focusing time, respectively. The amplitude of each component is given by:

$$a_n = \frac{A_{cr} S_n(\omega)\Delta\omega_n}{\sum_n S_n(\omega)\Delta\omega_n}, \tag{24}$$

where $\Delta\omega_n$ is the frequency increment, and $A_{cr} = \sqrt{2m_0 \ln(N)}$, where m_0 is the zeroth moment of the spectrum, is the linear crest amplitude. Evidence provided by investigation carried out by Whittaker et al. (2017) suggested that wave groups generated by wavemakers that move according to the NewWave linear theory may lead to the introduction of spurious waves into the generated spectrum. Furthermore, in light of the evidence provided in Mortimer et al. (2023), where high inaccuracies are found between first and second order based model for wave generation motion, the piston motion is corrected using second-order wave generation theory as developed by Schäffer (1996). Examples of focused wave validations with DualSPHysics can be found in Chow et al. (2022) or Tagliafierro et al. (2022d).

4. Validation

4.1. Free decay tests

The first validation we propose here comprises two time evolution comparisons that regard the surge and heave decay tests performed under the OC6-PhaseIa. Free decay tests allow in principle to assess the solver accuracy in evaluating the quality of the fluid–structure interaction, such as the hydrodynamic stiffness and the so-called added mass. They also enable an understanding of the quality of the two-way coupling technique employed to model the various elements involved in the simulation, such as the mooring system. The tests herein are performed by initializing the position of the system in the corresponding out-of-equilibrium posture that retraces the physically tested one. Lastly, all the numerical simulations are run with three different resolutions, respectively $P_T/4$, $P_T/8$, and $P_T/12$.

Fig. 5 proposes four charts into two columns that respectively show validation for the horizontal and vertical motion decay tests. In the first row of Fig. 5, the numerical time evolution motion of the CoG platform for the three resolutions is charted against the experimental one. The second row, synthetically charts the motion period computed using a zero-upcrossing technique and disregarding the first cycle for each data series.

The surge decay test, proposed in Fig. 5(a), overall shows poor agreement with the experimental time series. Two theories are here brought forward to explain the differences between the numerical model and experimental data for this specific test; some of the following considerations are also supported by results shown in heave decay test. First, the geometry of the float only comprises the bulkiest parts (the three pontoons and the central column) and the lack of the bracings which eventually provide different hydrodynamic properties (buoyancy and stiffness). Secondly, the different system mass, which complies with the specificity of the system being modeled, can partly contribute to this. Nevertheless, in terms of the simulated dynamic properties, the represented average period for the four events shown in the lower panel in Fig. 5(a) (i.e., $T_{s.num} = 14.40$ s versus $T_{s.exp} = 15.12$ s) provides a good enough validation for the behavior of this moored platform under lateral loads (error 5%). In principle, the great majority of the system recentering load is provided by the mooring system, which is pushed to experience very high deformations. On the negative side, in this test, the fluid-to-structure interaction between almost still water and the boundary particles shows high dissipation and the kinetic energy of the system in damped out in a very limited number of cycles, compared to the experimental ones. The diminished accuracy that the model has shown for this first test may be explained by two determining factors. In the first place, some setup discrepancies also highlighted in Section 3, may cause a difference in the perceived lateral fluid stiffness and added mass. Some similar behavior can be observed in Wang et al. (2022b)

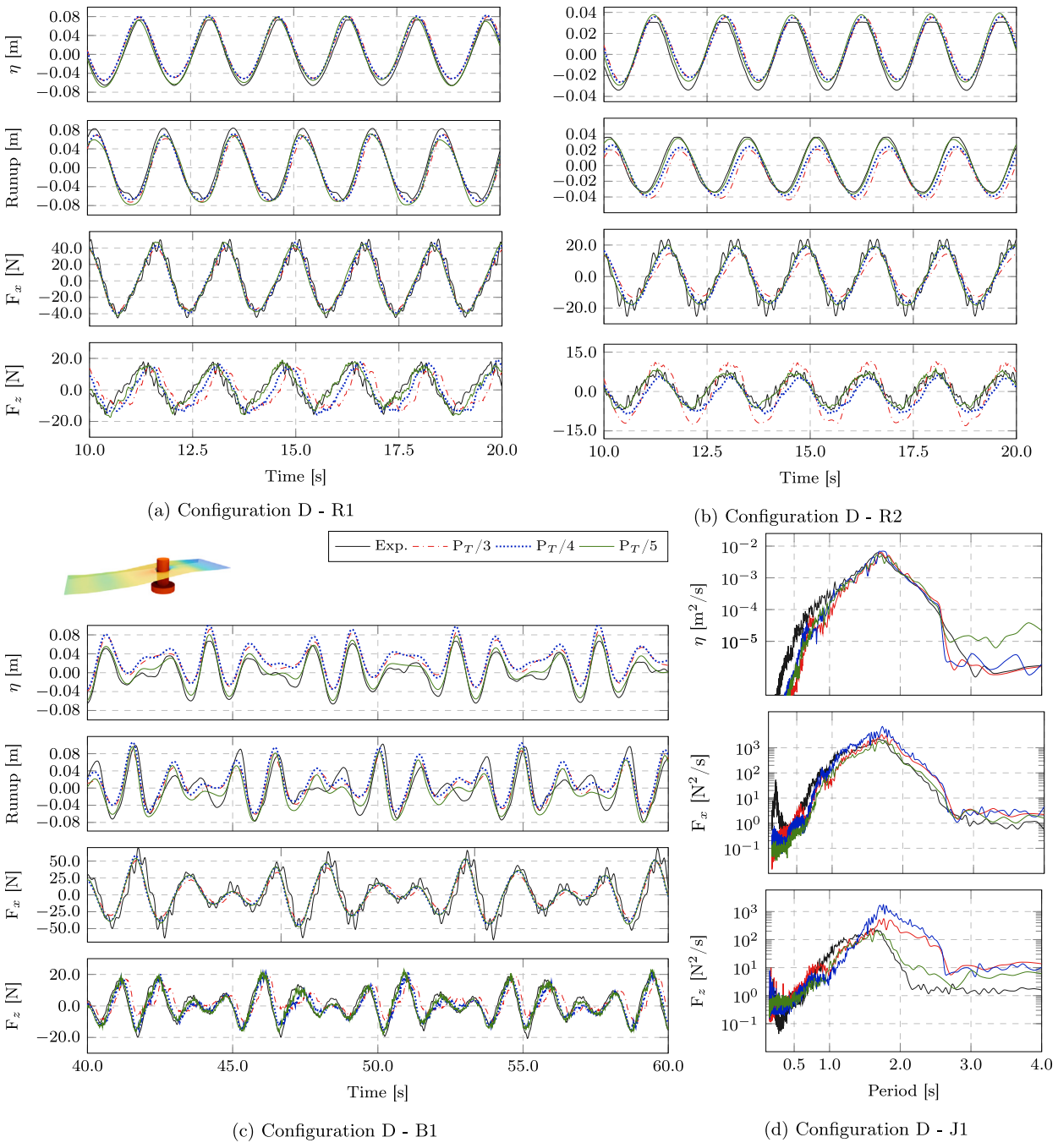

Fig. 6. Experimental vs. measured surface elevation, runup, surge and heave forces for configuration D.

or Li and Bachynski-Polić (2021), for some reported participants' results. The excessive damping ratio that is observed during the surge decay test (around 10% for the numerical response) usually shortens the observed cycling time, as the response of the system tends to be further apart from the natural period.

The heave decay test, proposed in Fig. 5(b), provides good matching against the experimental data for two of the three tested resolutions, with the coarser providing fair agreement for the first two cycles. It can be seen, by also comparing the period comparison that takes place in the second panel, the numerical average period ($T_{h.num}$ = 2.32 s) and the experimental ($T_{h.exp}$ = 2.39 s) are very close (error around 3% on the whole time series), meaning that for vertical induced motion, even of small amplitude (well below the smoothing length) is well captured. The amplitude of the motion is preserved throughout the test, with a dissipative behavior that appears when the amplitude of the motion reaches the size of the initial particle spacing. For the resolution $P_T/4$ (3.0 cm), the overdamped behavior starts when the oscillation amplitude is of about 3 cm (around the third cycle). It is also worth noticing that the numerical model correctly captures the period decrease that is likely caused by increasing hydrodynamic damping.

4.2. Hydrodynamic loads

As a subsequent stage for this research, the hydrodynamic performance of the SPH model is validated. The validation against the experimental data provided by the OC6-PhaseIb project is given for the three platform configurations reported in Table 5 subjected to four selected wave conditions reported in Table 7. The validations are arranged into integrated panels regarding each configuration divided

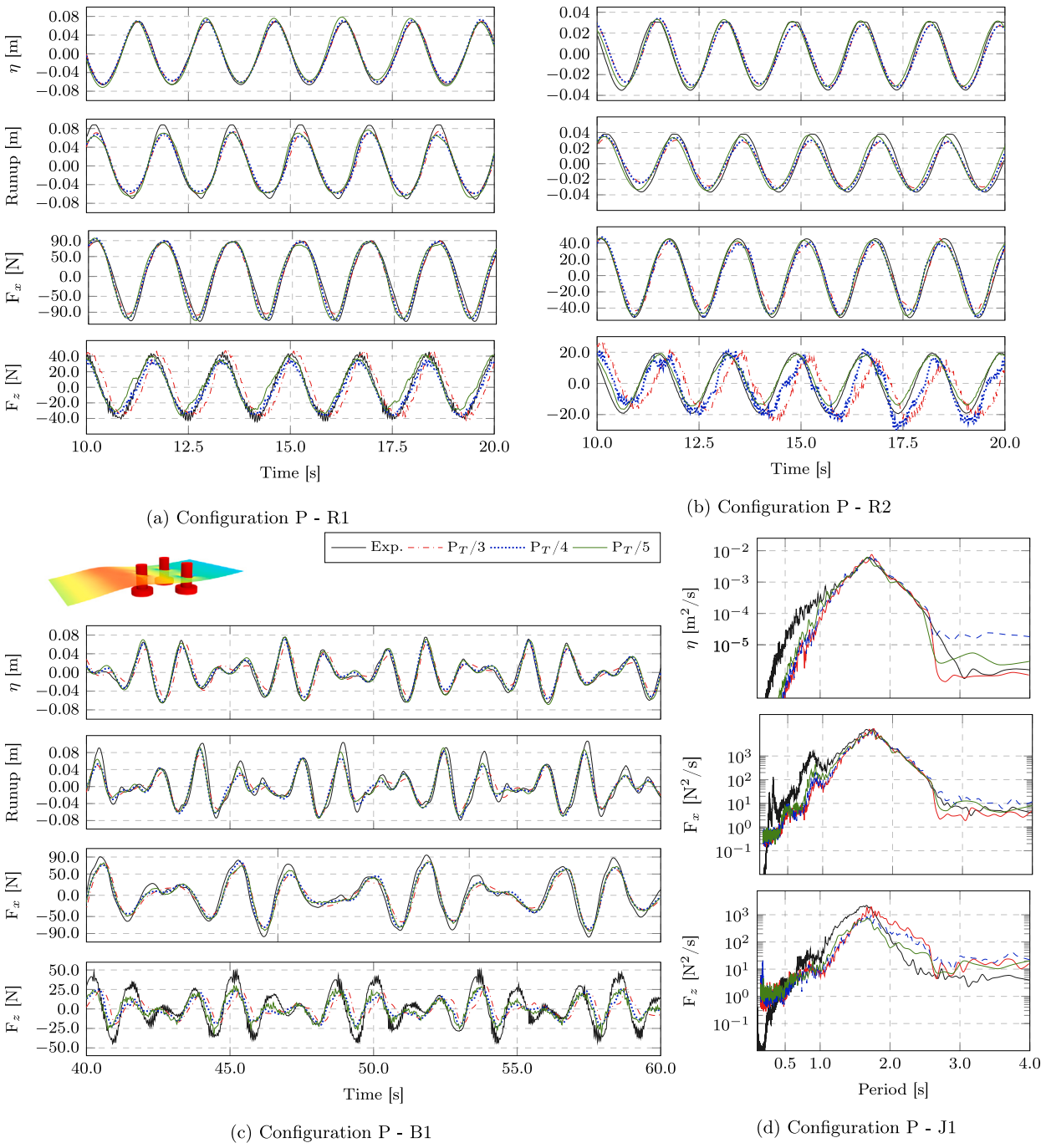

Fig. 7. Experimental vs. measured surface elevation, runup, surge and heave forces for configuration P.

into four sectors likewise the number of tested wave representations. Specifically for Fig. 6-Fig. 8, panel (a) reports the validation for case R1, (b) for case R2, (c) for case B1, and (d) for case J1. For each wave representation up to four panels are used to compare the model response in terms of surface elevation (gauged at Wave Probe in Fig. 3), run-up wave elevation for a probe located very close to the fore column (the distance changes slightly from case to case), and surge and heave forces (F_x and F_z, respectively) as measured by the load cell. Note that in the same fashion of what is done for the experimental data, the hydrostatic force is purged from the heave force. All the numerical simulations are run with three different resolutions, respectively $P_T/3$, $P_T/4$, and $P_T/5$. As the reader may have noticed, these three resolutions are determined independently of the results from the previous sensitivity study, as they are specifically chosen to account for WCSPH capability to capture pressure gradients. For gravity-driven phenomena, such as wave propagation, these selected resolutions prove to be appropriate.

Fig. 6 proposes the hydrodynamic validation for the configuration for the one column-plate configuration (Configuration D). For the regular wave R1, for a wave height almost close to the plate thickness, the surface and run-up numerical sensors provide fair agreement for all the resolutions, and the converge study shows little variation in the estimation of the water surface. The horizontal force pattern is well captured for all the tested resolutions, whereas the vertical force estimation shows to be sensitive to the particle resolution. This last occurrence may be partly caused by the high impact of the hydrostatic component on the total vertical force (i.e., 1000 N vs. 1100 N). For the regular wave R2, and to a similar extent for the bi-chromatic wave B1, in spite of having a halved wave height in comparison to R1,

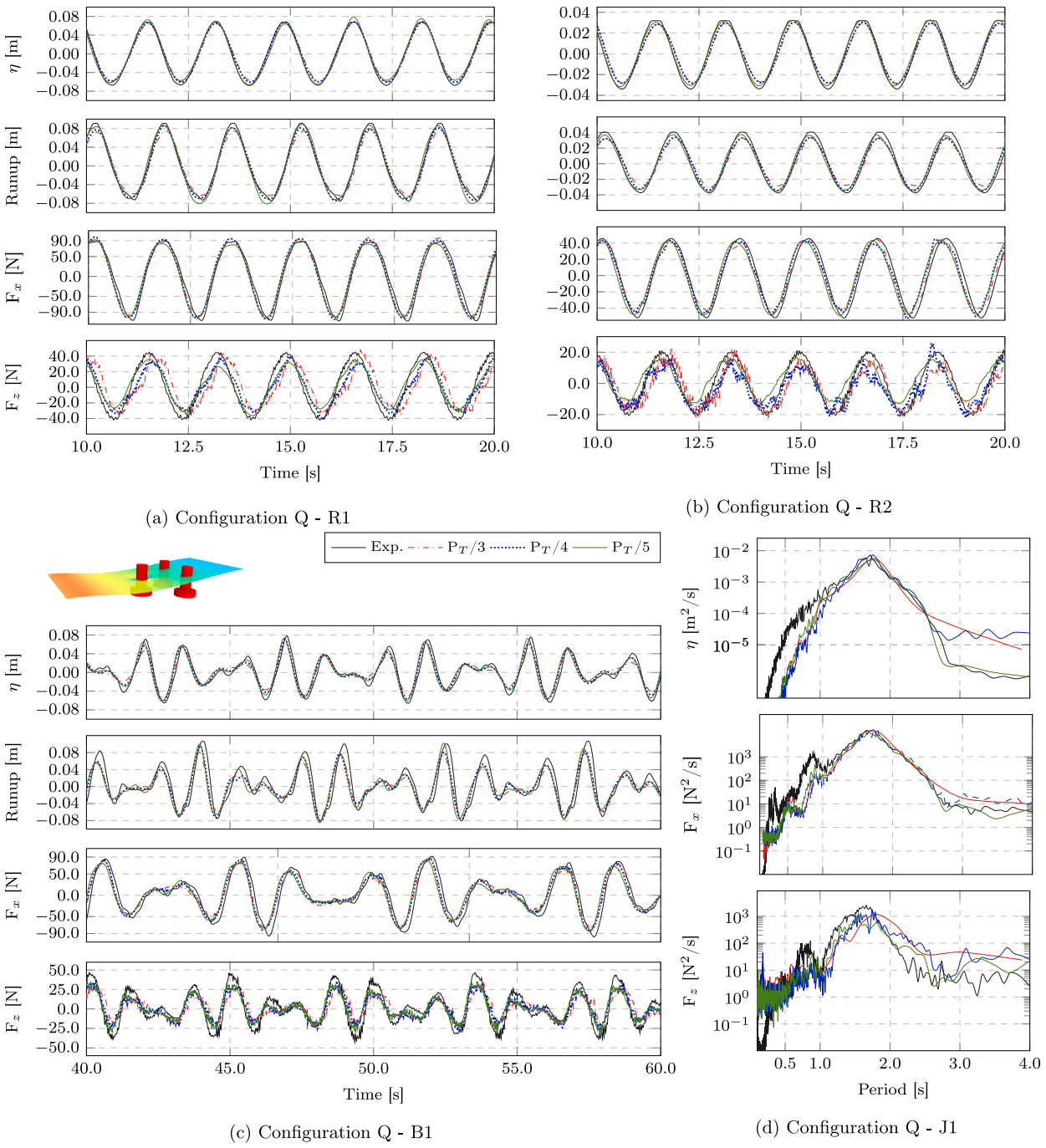

Fig. 8. Experimental vs. measured surface elevation, runup, surge and heave forces for configuration Q.

small discrepancies appear for the low resolutions. These discrepancies mainly take place in the estimation of the still water level (as evident from surface and run-up), which result in incorrect prediction of the induced loads. When the resolution increases, the model correctly captures the wave evolution, even for very short wave components (evident in bi-chromatic wave B1), that entails the correct estimation of the surge and heave forces. For the irregular wave model J1, the results are presented in terms of the spectral response. The model restitution is very accurate on account of almost all the significant components in the target spectrum; the surge force is very accurate for all the resolutions, whereas the heave force shows increasing quality as the resolution improves.

Fig. 7 proposes the hydrodynamic validation for the configuration for the full platform configuration (Configuration P), now with the three pontoons. The waves are captured with similar agreements to what was shown for the previous configuration D, with little differences across the values of employed resolutions. The wave induced forces, however, provide better estimation trends, especially for the vertical component of the fluid forces. This is partly due to the fact that for this configuration, the total force on the structure is used as reference. For very small wave components (R2 and B1) the highest resolution $P_T/5$ becomes critical to ascertain a good level of accuracy, especially for the estimation of the vertical forces. For irregular waves, the model shows very good agreement in estimating the most energetic part of the spectrum, capturing the magnitude of the peak force and its frequency, which closely corresponds to the incident wave content. A very interesting pattern, which forms in the force response spectra around 0.80 s is worth discussing. It appears as a secondary peak

in the force distributions (the numerical one has diminished energy content), which appears to be related to super-harmonic components (second order super-harmonic) and that may be exaggerated by radial refraction of the single pontoons. This further proves the capability of the employed CFD model to capture nonlinear phenomena that may take place when the structure interacts with ocean waves. However, the high frequency part of the reference spectrum for the free surface is not properly captured as its spectral energy content does not match the reference one. This may also be the cause for the diminished energy content in high frequency that is observed in the two force spectra.

Lastly, Fig. 8 proposes the hydrodynamic validation for the configuration for the full platform configuration with a negative five-degree tilt (Configuration Q). The accuracy proved by this comparison for the regular wave conditions R1 and R2 is very close to the one provided with the unmodified platform configuration. The wave profile is well captured by the three resolutions, much like the previous case, being the wave propagation only marginally affected by the presence of the platform. Small changes in shape of the wave through of the run-up sensor, which occur due to the diverse way the cylinder is oriented with respect to the incident wave, are captured by the numerical model, as evident for the R1 and B1, whereas due to a more linear response is generated by the wave–structure interaction in the case with R2. To capture the fluid-induced forces it is necessary, as proved during the previous tests, to move towards higher values of resolution. The F_x pattern is well captured by all the tested resolutions, whereas the F_z shows to be very sensitive to the SPH resolution. As remarked above, the value of F_z reported in the comparison accounts for the increment in pressure caused by the wave propagation, which results in magnitude oscillation in the order of 10% of the hydrostatic pressure. For the irregular wave J1, the precision in the surface elevation remains unchanged and again below the SPH resolution. The tested numerical model can almost exactly match the horizontal force for a wide variety of components, capturing the main peak and the two minor peaks that respectively occur at 0.85 s and 0.55 s. The vertical force power density spectrum also shows good matching with the reference one for the most energetic part of it.

As mentioned earlier for wave condition J1 on Configuration P, the free surface spectrum is again not properly captured in the high frequency band, showing a consistent onset. These may be induced by a reduced number of waves considered for these two tests when compared with J1 for Configuration D. This information is provided in Table 7. For Conf. D, the wave train comprises 1000 waves and this may have lead to a much closer spectrum than the one generated with 500 waves, as for Conf. P and Q.

Pressure validation

An additional proof of validation is provided considering the fluid pressure estimation on the fore column for Configuration P and wave condition R1. Results are reported in two panels in Fig. 9, comprising a still model convergence study with the three predefined resolutions. The location of the two pressure gauges is depicted in Fig. 4. Fig. 9(a) compares the model pressure response at the pressure sensor code-named UF4, located with a free board of 7.5 cm. The sensor experiences cycles of dry/wet conditions as it is highlighted in the chart, in which values of pressure peak at around 750 Pa, alternated to very low pressure (close to zero) when the wave through approaches the structures. The numerical model shows a clear convergence trend, with a more consistent response with the highest resolution. Although the highest resolution clearly undershoots the maximum values, this behavior is somewhat expected as the numerical runup sensor in Fig. 7 shows a little underestimation on the height of the crest. Fig. 9(b) compares the pressure time evolution for the sensor BF4 located on the upward surface of the plate (−0.24 m) and 12 cm apart from the column. In this case, the model shows very good accuracy and with small variation in crest and through induced pressure magnitudes.

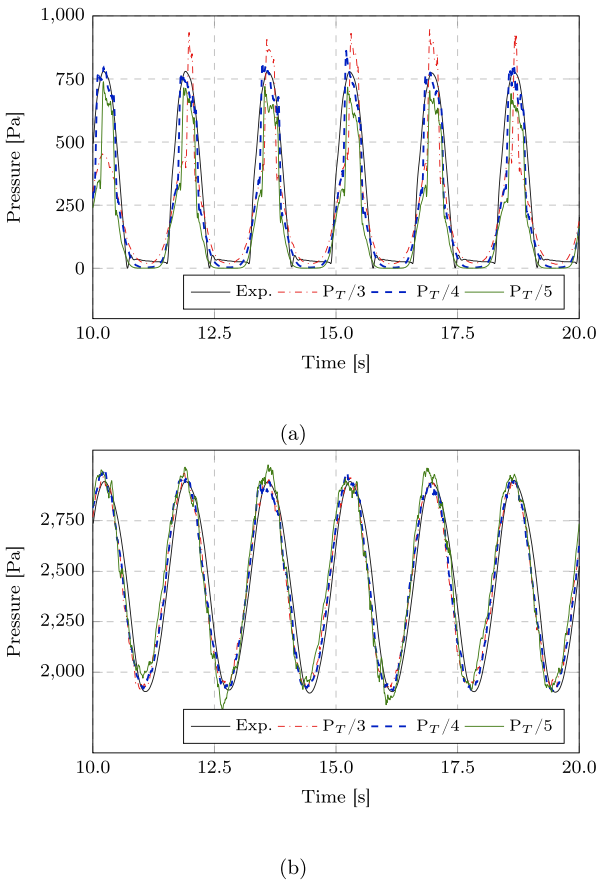

Fig. 9. Experimental vs. measured pressure at (a) UF4 and (b) BF4 for the Configuration P under R1.

5. Investigation: focused waves

The previous section demonstrated the capabilities of DualSPHysics in simulating semi-submersible platforms for floating wind. Firstly, we validated the motion of the floating rigid body during decay tests. Secondly, we analyzed the wave loads on a fixed version of the substructure. In the present section, we aim to simulate the complete system, focusing on the response of the FOWT under wave action. We explore a novel wave representation to enhance our understanding of the performance of floating structures in severe and extreme events. A significant motivation for this stems from recognizing that in presence of extreme environmental loads, the response of FOWTs is primarily influenced by wave-induced actions, surpassing aerodynamic forces, as posited by Muliawan et al. (2013).

5.1. Wave conditions

Focused waves offer several advantages as a wave representation. They not only provide a convenient and efficient means of capturing highly energetic wave-structure interactions (Tosdevin et al., 2023; Tagliafierro et al., 2023a), but they are also characterized by their brevity, resulting in lower simulation costs for both numerical and experimental setups. It is worth noting that the natural heave period of the SFP typically falls below the range of wave periods for normal operational sea states. However, under extreme sea states, the wave period aligns more closely with the dynamic properties of such platforms (DNV-ST-0119, 2021). Consequently, special tools, particularly CFD models, have gained popularity for simulating extreme wave conditions. A recent study has specifically examined the application

Table 8
Focused waves parameters for the test matrix **F1**. The water depth is set to 1.20 m.

	A	B	C	D	E	F	G	H	I	J	K	L	M
$A_{cr}(x_f)$ [m]	0.10	0.12	0.14	0.16	0.18	0.20	0.22	0.24	0.26	0.28	0.30	0.32	0.34
T_p [s]	1.88	1.88	1.88	1.88	1.88	1.88	1.88	1.88	1.88	1.88	1.88	1.88	1.88
x_f [m]	9.77	9.77	9.77	9.77	9.77	9.77	9.77	9.77	9.77	9.77	9.77	9.77	9.77
ϵ [-]	0.129	0.154	0.180	0.206	0.232	0.257	0.283	0.309	0.334	0.360	0.386	0.412	0.437

Table 9
Focused waves parameters for the test matrix **F2**. The water depth is set to 1.20 m.

	A	B	C	D	E	F	G	H	I	J	K	L	M
$A_{cr}(x_f)$ [m]	0.10	0.12	0.14	0.16	0.18	0.20	0.22	0.24	0.26	0.28	0.30	0.32	0.34
T_p [s]	1.48	1.60	1.70	1.79	1.88	1.96	2.03	2.11	2.17	2.24	2.30	2.36	2.42
x_f [m]	6.66	7.55	8.36	9.09	9.77	10.40	10.98	11.53	12.05	12.55	13.01	13.46	13.89
ϵ [-]	0.189	0.200	0.210	0.221	0.232	0.242	0.252	0.261	0.271	0.280	0.290	0.299	0.308

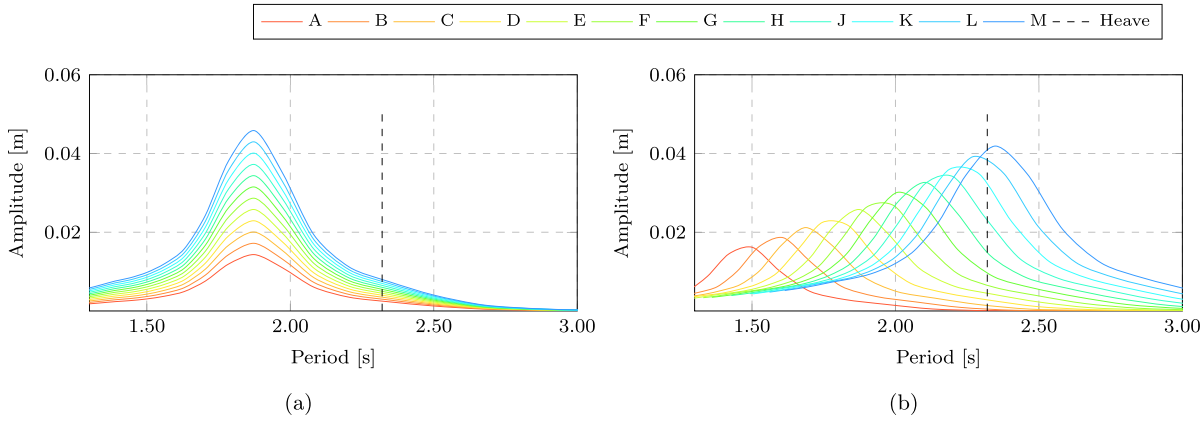

Fig. 10. Spectral representation of the focused wave surface for the two test matrices **F1** and **F2**.

of focused waves in estimating higher-harmonic wave loads and low-frequency resonance on the DeepCwind platform (Zeng et al., 2023a). This research contributes to the existing body of knowledge supporting our current investigation.

Two test matrices are set for this study and presented in Tables 8 and 9, respectively. Both test groups comprise 13 sea states each, which are defined in accordance to the parameters that are needed for focused wave generation. The two sets are created in order to ideally represent the boundary of environmental contours as defined in Anon (2009), and similarly to what was investigated in Shahroozi et al. (2022). In **F1**, each sea state has a wave crest height at the focusing location, $A_{cr}(x_f)$ increased by 2 centimeters, however preserving the same peak period T_p. In **F2**, the same wave heights values are used but this time the peak period is assumed to comply with an hypothetical Rayleigh distribution and as such, it is increased in a exponential fashion (see, Anon, 2009). Additionally, the two tables indicate the focusing distance (x_f), taken as twice the theoretical wavelength and corresponding to the distance between the platform CoG and the wave paddle, and the wave steepness (ϵ).

The remaining shared parameters for the generation of the paddle motion for the focused wave groups are: the number of components, $N = 256$, (Whittaker et al., 2017; Ransley et al., 2017); the target JONSWAP power density spectrum with a peak period T_p and a significant wave height H_{m0} ($\gamma = 3.30$). Lastly, the obtained theoretical surfaces are spectrally represented in Fig. 10, in which the two panels respectively refer to test matrix **F1** and **F2**, and for the sake of comparison, the heave period is reported as well. The simulations are carried out considering the wave basin in Fig. 3. Specifically, the parameter that defines the length of the 3D domain, L_X, complies with the focus distance x_f, whereas the water depth corresponds to 1.20 m (Tagliafierro et al., 2023b). All the tests are run with the resolution $P_T/5$, to guarantee the maximum model fidelity regarding the wave force estimation. Due to high dissipation demonstrated during the surge decay tests, the behavior of the platform in the tail of our simulations is disregarded.

5.2. Floater motion and mooring line dynamics

Prior to scrutinizing the results of the two test matrices, one simulation is analyzed in detail for a better understanding of the model variables under investigation. The chosen setup employs the wave conditions corresponding to Case **E**, which appears in both investigations with the same parameters. In Fig. 11, four charts show the captured data from the numerical model. Panel Fig. 11(a) validates the wave generation and propagation capability of the model setup, for which the surface elevation (from still water) is sampled at the focusing point and compared with the theoretical solution obtained from the NewWave theory (Tromans et al., 1991). The wave profile that reconstructs at the focusing location compares quite well with the theoretical solution. Fig. 11(b) and Fig. 11(c) report the surge and heave platform motion and the total fluid force evolution, respectively. Lastly, Fig. 11(d) proposes the dimensionless line tension, T/T_{still}, experienced by the fore and port connections. Here, T_{still} is the line tension from the still water test.

The last three plots in Fig. 11 highlight the relationships that establish between the platform motion and the line forces. Being more deformable in surge, the platform displaces remarkably along the wave propagation direction, whereas the heave motion remains under a ±0.05-meter threshold. In terms of frequency response, the surge motion contains short components that are due to the external force frequency, being in fact the response of the system dominated by its inertia (force frequency around 0.50 Hz, natural frequency of the system around 0.05 Hz). Long components are present in the surge motion, which yields a consistent misalignment from its rest position. The heave force, instead, shows a very stiff behavior with small oscillations around

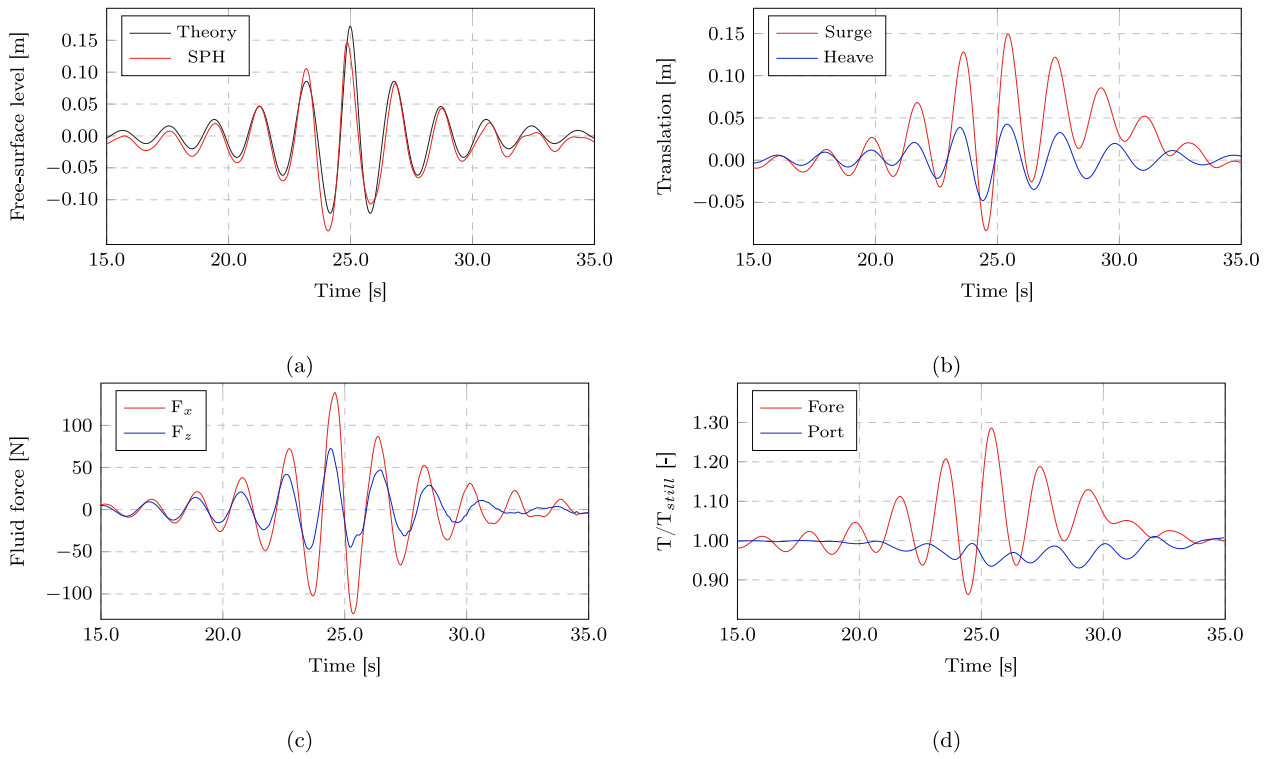

Fig. 11. Test results for the focused wave condition **E**: (a) free-surface elevation validation; (b) platform motion; (c) dimensionless tension in the mooring system; and (d) fluid force components on the platform.

the equilibrium position. Having this in mind, understanding the line tension response is immediate. For the particular arrangement of the mooring line and the wave direction, the fore line takes the brunt of the hydrodynamic-induced loads, whereas the port (and the starboard) lines even appear to slightly reduce their internal stress.

The eight frames in Fig. 12 assemble a sequence that shows the moored platform engaged by the main peak of the focused wave in Case **E**. The fluid surface is rendered using coloring proportional to the velocity magnitude, and the platform with solid gray. Overall, it can be seen how the free-board in the fore column is greatly challenged by the wave crest, which hence passes through without inducing any green-wave effects on the structure. Note that the crest height seems to increase as it approaches the platform, and this is a feature of focused waves as the main peak builds in time at the designated location as a sum of the generated components. It is worth mentioning that the wave focusing position, x_f, is designated accounting for the CoG position of the platform at rest. However, it is easy to see that this is not the case, as the condition is not precisely met due to the platform unknown displacement. Nevertheless, the coincidence of x_f with a specific point is only for convenience of setup.

Fig. 13 organizes the results of the two test matrices **F1** and **F2** into six panels, in which the most significant gloabal model quantities are charted. Data regarding **F1** is reported in the first column, whereas **F2** is reported in the latter. As a reminder, the two sets represent two ways to discretize the environmental contours. All the panels report data by contrasting the processed magnitude against the maximum wave amplitude of the generated focus wave groups (x-axis). In Fig. 13(a), the peak response of the platform surge, heave, and pitch is reported; Fig. 13(b) shows the dimensionless tension peaks in the fore mooring line, arranged into three groups accounting for the competing wave taken from the wave group. Specifically, *Preceding* and *Following* refer to the wave peaks that precede and follow the main crest (*Crest*). Fig. 13(c) plots the maximum values of fluid force components on the hull referred to the global reference system. There are two maxima per each component worth investigating here respectively, the one that comes from the time series maximum force (operator defined as max(F)) and the fluid force when the paired displacement magnitude peaks (operator defined as F|max(motion)). Note that for the F_x, only the magnitude is considered.

Clearly, the results in Fig. 13 show a consistent increase in the wave induced forces when the focused wave parameters are representative of more energetic sea states, even though providing different patterns according to the wave characteristics. By comparing the overall trends that form in **F1** and **F2**, the load effects on the components of the FOWT are greatly related to the longitudinal component F_x of the wave force (external force).

For **F1**, a nearly linear response can be observed in terms of the maximum surge motion, the horizontal fluid force, and the maximum line tension for the three primary peaks of the wave train. The vertical fluid force, which faces significant opposition from the hydrodynamic and anchoring system stiffness, consistently results in a steady and constant increase in the maximum heave motion. Regarding wave steepness, the chart indicates that extreme steep waves ($\epsilon > 0.30$) may lead to highly nonlinear effects in the system response due to the increased likelihood of wave breaking. Additionally, the platform's seemingly different position prior to wave impact contributes to this nonlinearity in a global sense. These effects are particularly evident in the surge and pitch motion, which are directly influenced by longitudinal wave forces. Starting from Case **J**, the wave-induced effects no longer exhibit direct proportionality to their cause. Instead, they are amplified due to some overtopping experienced by the fore column. This is remarked in the chart by the label *runover* that indicates the point when the waves are overrunning the platform columns.

F2 shows an almost inverse behavior when compared to the former **F1**. Firstly, it is important to note how the horizontal and vertical forces climb at constant, and almost similar pace. The platform motion, and the strongly related fore line tension behave in linear fashion starting from Case **D**. Despite displaying similar maximum surge displacements, the heave and the line tension show a much higher rate of increase when compared to **F1**. By comparing with the wave-induced pattern

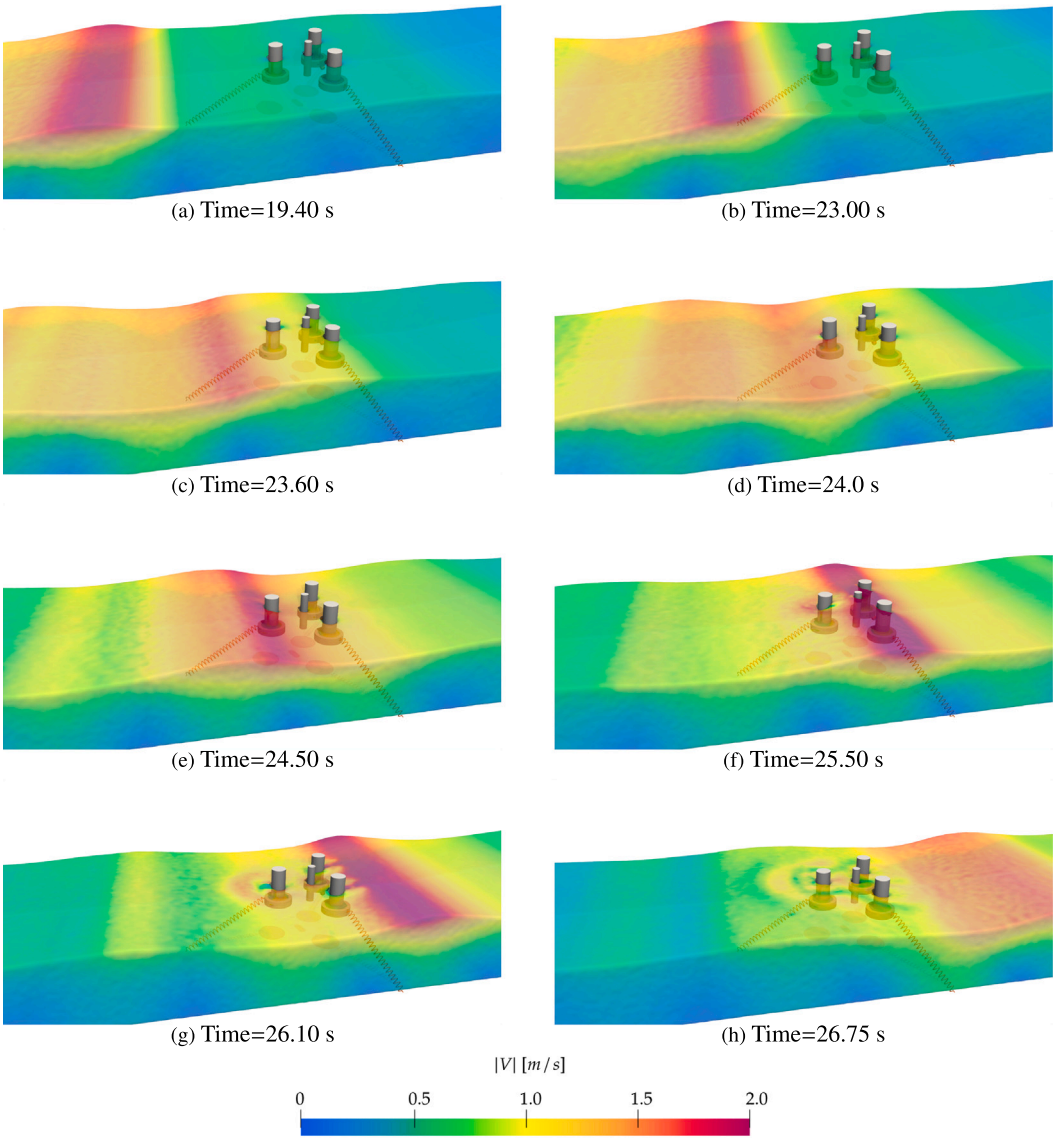

Fig. 12. Snapshots of the platform simulation under focused wave **E.**

of the former case, the greater line tension can directly result from the more pronounced heave motion, which must be caused by the wave frequency closing up with the resonance period in heave (ref. Fig. 10). Insofar as the wave-induced effects are concerned, higher loads are experienced when the frequency content approaches the system's period of vibrations. The results proposed in the three charts prove also that wave steepness cannot alone be used to identify severe conditions. Similar trends are suggested by other research investigations on the behavior of moored floaters under steep waves (Katsidoniotaki et al., 2021; Shahroozi et al., 2022).

Fig. 13(c) additionally shows how the maximum fluid force horizontal and vertical components are not peaking when the surge motion (and the fore line tensions) does, as proven by the lines that refer to max(F) and the F|max(motion). This fact together with the occurrence of maximum line tensions pairing up with maximum displacements sets a particular circumstance that is relevant to the Ultimate Limit States (ULS) safety checks. Reportedly, local stress verification on the platform hull structural components and the fairlead connections must always consider the most unfavorable conditions. Now, the patterns that the line tension and the fluid loads (pressure) form indicate that performing one check that involves the peak *effects* would not be ideal. First, due to the fact that the maxima are not in sync, the check will lose meaning in a physical sense, as that combination of loads is never experienced by the structure. Secondly, due to very big difference between max(F_z) and F_z|max(Heave), which in some cases is almost 80% in favor of the former, can lead to costly over-design practices.

5.3. Hydrodynamic loads

As evidenced by the results proposed in the prior global analysis, the understanding of fluid mechanics near offshore platforms is vital for the effective design and operation of FOWT. High-fidelity software capabilities can be harnessed to conduct detailed investigations into the hydrodynamics and investigating the pressure distributions enables us to gain valuable insights into the dynamic interactions between the waves and the fore column, contributing to a more comprehensive understanding of FOWT behavior in extreme sea conditions. Previous investigations have examined similar semi-submersible platforms under highly energetic sea conditions, offering valuable insights into the platform response during such events (Zhou et al., 2019; Zeng et al., 2023a,b). Our work builds upon these studies by providing a deeper understanding of the local hydrodynamics, specifically focusing on wave overtopping and breaking waves in the presence of incremental focused waves.

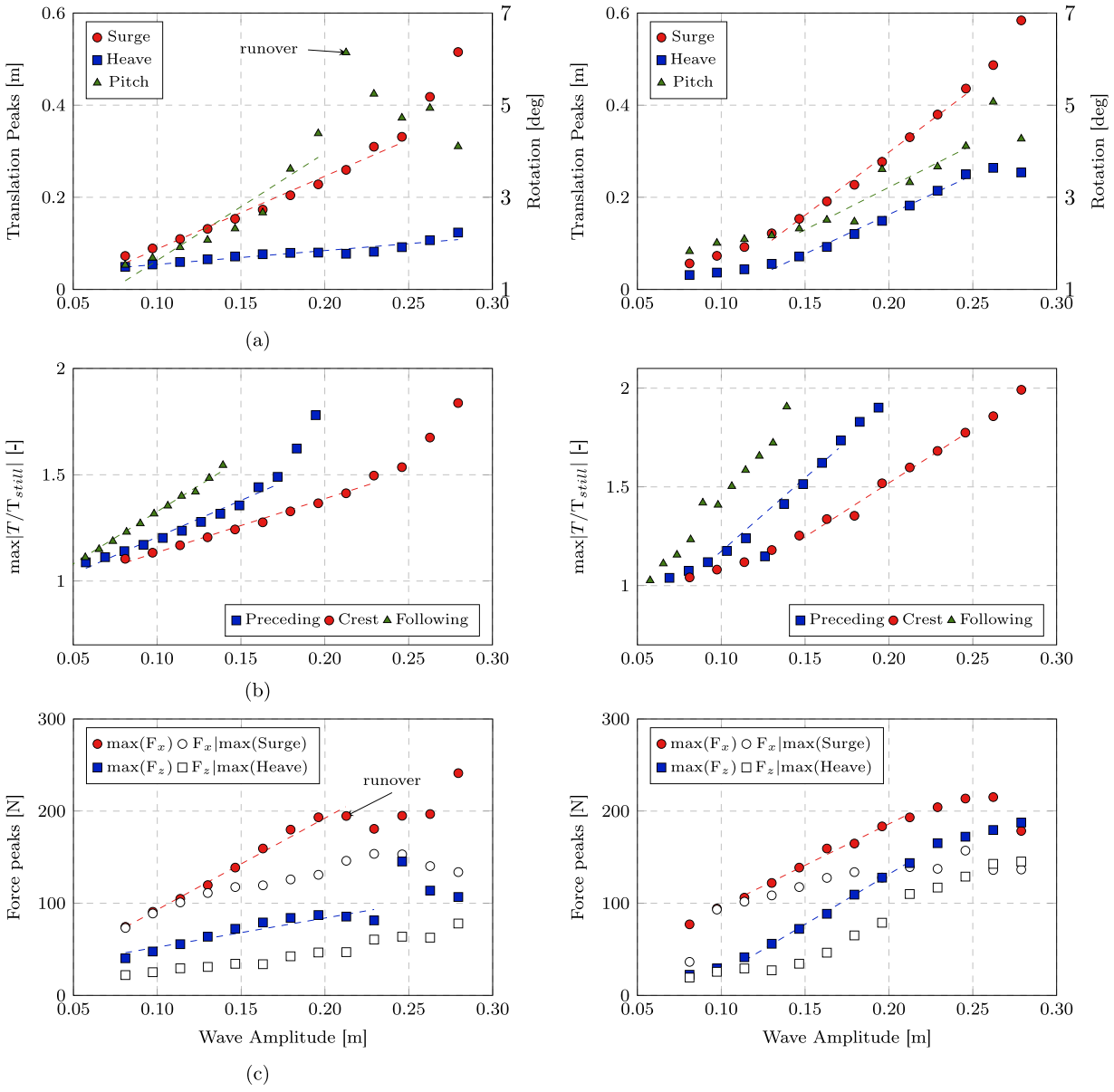

Fig. 13. Peak response investigation for the test matrices **F1** (left column) and **F2** (right column). Platform motion (a), line tension peaks (b), and fluid force components on the hull (c).

Pressure

In this study, we focus on a significant factor – the induced pressure onto the fore column. In Fig. 15, the pressure profiles that arise from probing locations indicated in Fig. 14 is presented for the fore column exposed to the waves in two test matrices, denoted as **F1** and **F2**. The line colors correspond to specific cases (A to M) based on the nomenclature employed in defining the test matrices. The hydrostatic pressure measured in still water conditions is represented by the dashed black line, here included to facilitate the visual comparison. The time evolution of pressure is indicated in the following as P(t).

Fig. 15 is divided into three sub-panels, which respectively report: (a) and (b) the envelope of the maxima registered at each pressure gauges throughout (max(P(t))); (c) and (d) the pressure profiles when platform heave motion registers its maximum (P(t|max(Heave))); and (e) and (f) pressure distributions when the maximum pressure value is recorded (P(t|max(P))). Note that the chart directionality considers wave incoming from the left-hand side of each panel. Overall, the data reported in the 6 charts clearly indicates the positive correlation between wave height and measured pressure, which confirmed for all the cases in **F2** (non-steep waves), whereas some variations can be appreciated for some cases in **F2**.

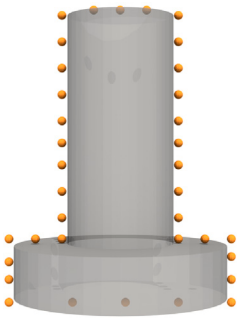

Fig. 14. The orange spheres mark the positioning of the numerical pressure gauges utilized on the fore column.

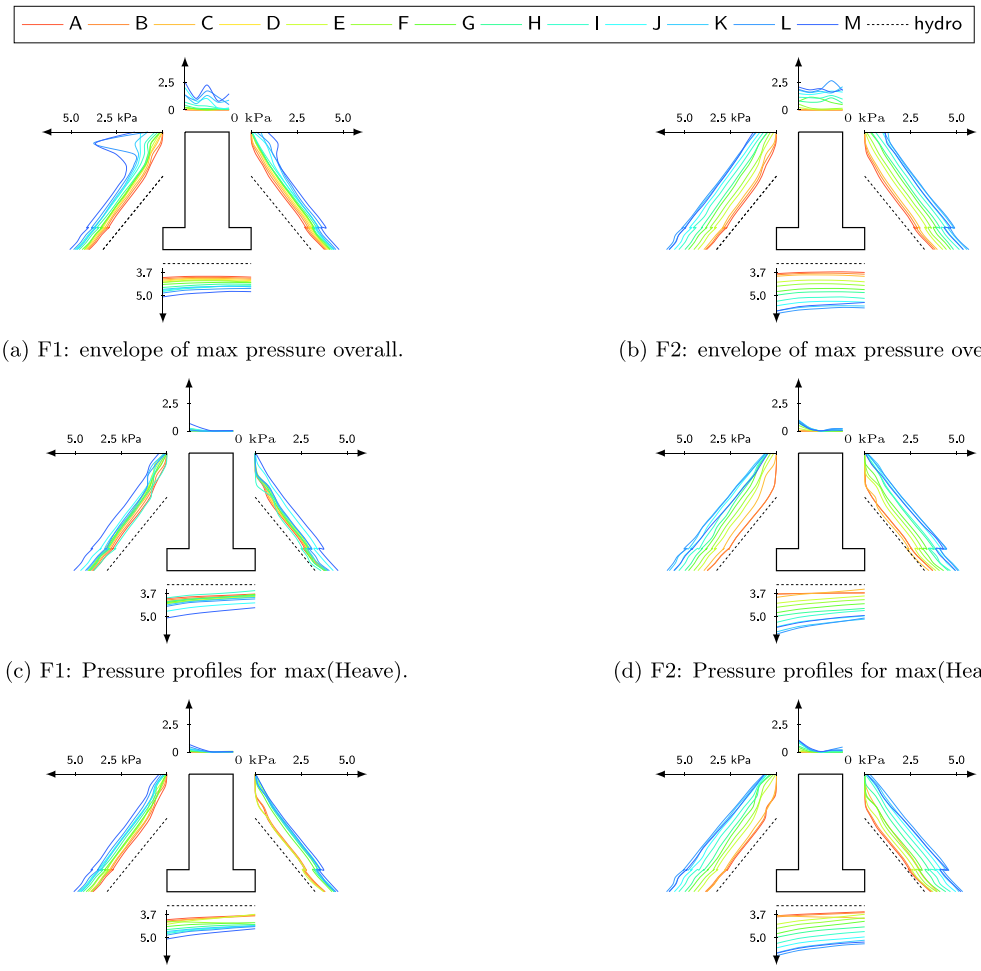

(a) F1: envelope of max pressure overall.

(b) F2: envelope of max pressure overall.

(c) F1: Pressure profiles for max(Heave).

(d) F2: Pressure profiles for max(Heave).

(e) F1: Pressure profiles for max(Pressure).

(f) F2: Pressure profiles for max(Pressure).

Fig. 15. Pressure distribution over the fore column for the two test matrices **F1** and **F2** (all the values are expressed in kPa).

In Fig. 15 (a) and (b), the maximum overall pressure values are presented, forming an envelope of maxima, and as such, the information in the two charts is independent of time. Comparing the pressure loads induced by waves with higher steepness (left) on the side facing the incoming wave, they result in very high loads on the column's freeboard, suggesting an impulsive load likely caused by wave breaking. Conversely, the downstream side shows pressure distributions that closely follow hydrostatic conditions, considering the time-varying free surface. For test matrix **F2**, the pressure maxima align with loads induced by pure hydrostatic considerations, with maximum pressure exceeding **F2** by over 25% in more extreme cases. Overall, pressure values are observed on top of the column, describing specific instances of wave runup and overtopping.

In Fig. 15 (c) and (d), a snapshot of the pressure profile during the peak heave magnitude is presented, revealing two distinct patterns. For **F1**, a chaotic situation is observed, with a loss of correlation between wave height and maximum load, particularly evident for cases with lower wave amplitudes. Interestingly, the extreme loads experienced by the freeboard do not coincide with the peaks of heave (or surge). In contrast, the results for **F2** resemble the previously investigated conditions, displaying overall maxima.

Lastly, in Fig. 15 (e) and (f), each panel displays a snapshot of the simulations when the pressure peaks. As expected, the maximum pressure value occurs at the bottom of the plate for both cases, showcasing shapes closely related to hydrostatic distributions. This indicates that the pressure maximum on the hull is achieved when negative heave values occur, leading to increased draft values.

For all purposes, the three load configurations considered here highlight the importance of wave steepness in identifying relevant load cases for structural safety checks. One should always consider circumstances when the displacement is maximized (resulting in mooring loads) along with cases when the hydrodynamic pressure on the hull is maximized. For mild waves, the circumstances depicted in Fig. 15 (b), (d), and (f) provide almost similar operative conditions, allowing the worst-case scenario to be easily framed in a *linear* sense. However, when steep waves are expected, the relationship between loads and displacement becomes weaker, and the local hydrodynamic evolution needs to be carefully considered.

Vorticity

In the upcoming investigation, we will focus on examining the underlying hydrodynamics of wave impacts on the platform, specifically considering the wave setups corresponding to L from **F1** and **F2**.

Each panel in Fig. 16 presents a contour plot in the time-spatial domain, derived from a series of free surface time snapshots taken at regular 1-cm intervals and sampled at 20 Hz. The color representation indicates the deviation of the free surface from the still water level. Both waves share the same critical amplitude (A_{cr}) but have different wave periods (yielding different steepness). In Panel (a), representing the first wave characterized by higher steepness, the main crest, easily identifiable by a gray circle at the focusing time and location (starts at 20 s), exhibits less pronounced peaks. Additionally, the preceding crest shows a higher wave elevation than the main crest itself. On the other hand, Panel (b) highlights much more consistent and pronounced wave

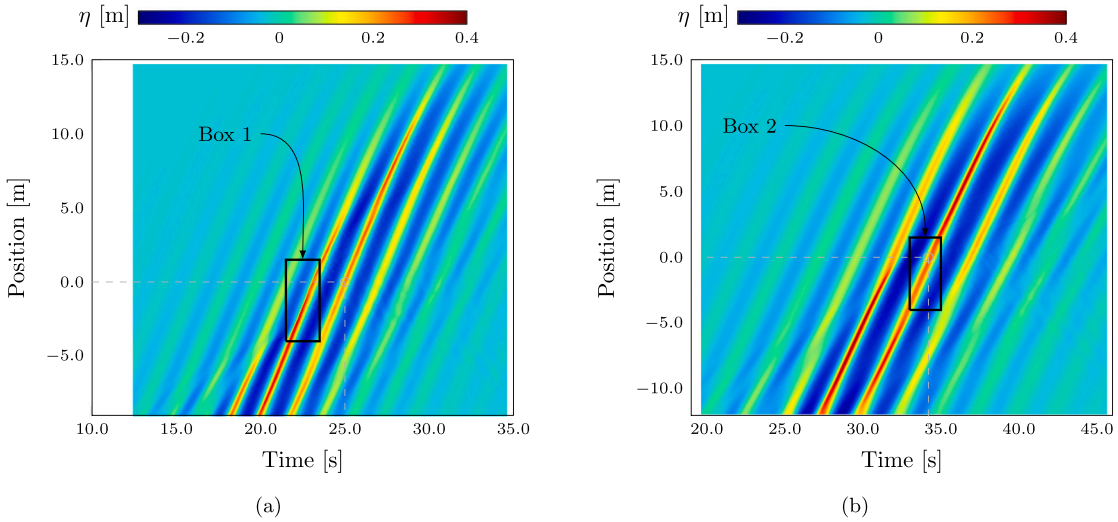

Fig. 16. Temporal and spatial evolution of the free surface for the Case *L* in **F1** (a) and **F2** (b). The gray circles indicate the focusing time and location. Box 1 and Box 2 serve as a time-space reference for Fig. 17(a) and Fig. 17(b), respectively.

profiles that propagate smoothly with minimal interference among various crests. The two boxes (Box 1 and Box 2) provide indications of where and when the next investigation is carried out.

Fig. 17 presents the reconstructed y-component of the vorticity field across the vertical mid-plane (x-z) that intersects the fore floater. The data corresponds to the two previously analyzed cases: Case *L* in **F1**(a) and **F2** (b). Specifically, the vorticity field is shown for the time-space windows Box 1 and Box 2 as indicated in Fig. 16. In columns (a) and (b), there are nine frames each, with the simulation advancing by 0.25 s for each frame. The solid black line in each frame represents the free-surface interface. It is important to remark that the discernible deviation between the position of the free surface and the actual position of fluid particles above it. This discrepancy is a direct outcome of how the free surface is identified, as explained before in Section 3.

In Fig. 17(a), the initial frames illustrate the approaching crest with excessive steepness, leading to wave breaking as evident from the formation of a macro-vortex nearby the wave front. During this phase, the platform remains relatively still since it is the first wave to impact it. Remarkably, in the third and fourth frames, the wave crest plunges and generates a highly turbulent velocity field. As we progress to the fifth frame, the wave crest impacts and overruns the fore column, also hitting the central column in the sixth frame, resulting in complex hydrodynamics around the hull. However, the starboard side (neither the port) has not yet been reached by the most energetic part of the wave, which occurs in frames seven and eight, leading to lower fluid-induced loads on the fore column. Throughout the frames, one can observe the formation of vortices induced by the advancing breaking crest (of significant importance) and the motion of the float (of minor importance).

The first frames in Fig. 17(b), in which the main crest is approaching the platform, the wave profile this time appears to be much smoother, owing to the much longer wavelength. Now, the wave is capable of inducing runup over the first floater much sooner given the disadvantageous position prior occupied by the platform, and induced by the preceding crest. The wave is capable of completely engulfing the platform (fifth to seventh frames), which may be one of the worst conditions for the design of the mooring system due to high buoyancy combined with diminished heave hydrodynamic stiffness. In this sequence, the vortices are mainly provoked by the relative motion between the hull and the fluid, whereas little to no energy intensity is induced by the local wave kinematics.

The analysis of the results presented in this section can be better understood in light of the conclusions drawn in Section 5.2. The occurrence of maximum pressure serves as a useful indicator for identifying other limit states for the hull. In cases where waves have milder profiles, such as those in **F2**, the most restrictive load condition can be determined using the maximum heave motion of the platform. This is evident in Fig. 15 (b,d,e), where the pressure distribution closely aligns with the envelope of maximum values. Only one condition is left unaccounted for here, which pertains to the maximum loads induced on the top column. However, in the case of steep waves (**F1**), the hydrodynamics resulting from a breaking wave front impacting the freeboard of the columns makes it more challenging to identify the most restrictive case. While considering the total horizontal forces in Fig. 13 for both test matrices, the one identified earlier could suffice. Nevertheless, local pressure on the freeboard are much more pronounced, with spikes increasing up to 100%, as shown in Fig. 15(a).

6. Conclusions

A validation study has assessed the accuracy of a mesh-less based numerical method in reproducing a very complex fluid-solid interaction that regards the renewable energy sector. We have presented a complete validation for the weakly compressible SPH method in estimating surge and heave dynamic properties and in evaluating the hydrodynamics loads induced by different wave representations on the moored DeepCwind platform.

The surge decay test has provided a measure of the accuracy of the employed method that remains acceptable within engineering applications ($\approx$ 5%), whereas the heave decay test has proven much more accurate in predicting the overall system frequency with an average error well within a 3%-range. From the response damping, it can be concluded that the SPH implementation, as it stands, induces excessive numerical dissipation when non-gravity-dominated phenomena are involved, which may result from the concurrent use of a density diffusion formulation employed. Within the tested period range, the estimated damping slightly depends on the oscillation period, whereas an extensive dependence on the oscillation amplitude is observed. However, the investigated model resolutions showed consistent and convergent trends for the two free-decay tests, which in principle highlights the model's potential precision.

The investigation into hydrodynamic loading on floating offshore wind substructures has yielded good accuracy. It is worth noting that this research represents the first time such an investigation has been conducted using open source and freely accessible CFD-based software (Wang et al., 2022c, 2021). The model has demonstrated high fidelity in predicting wave loads and local wave transformation for both

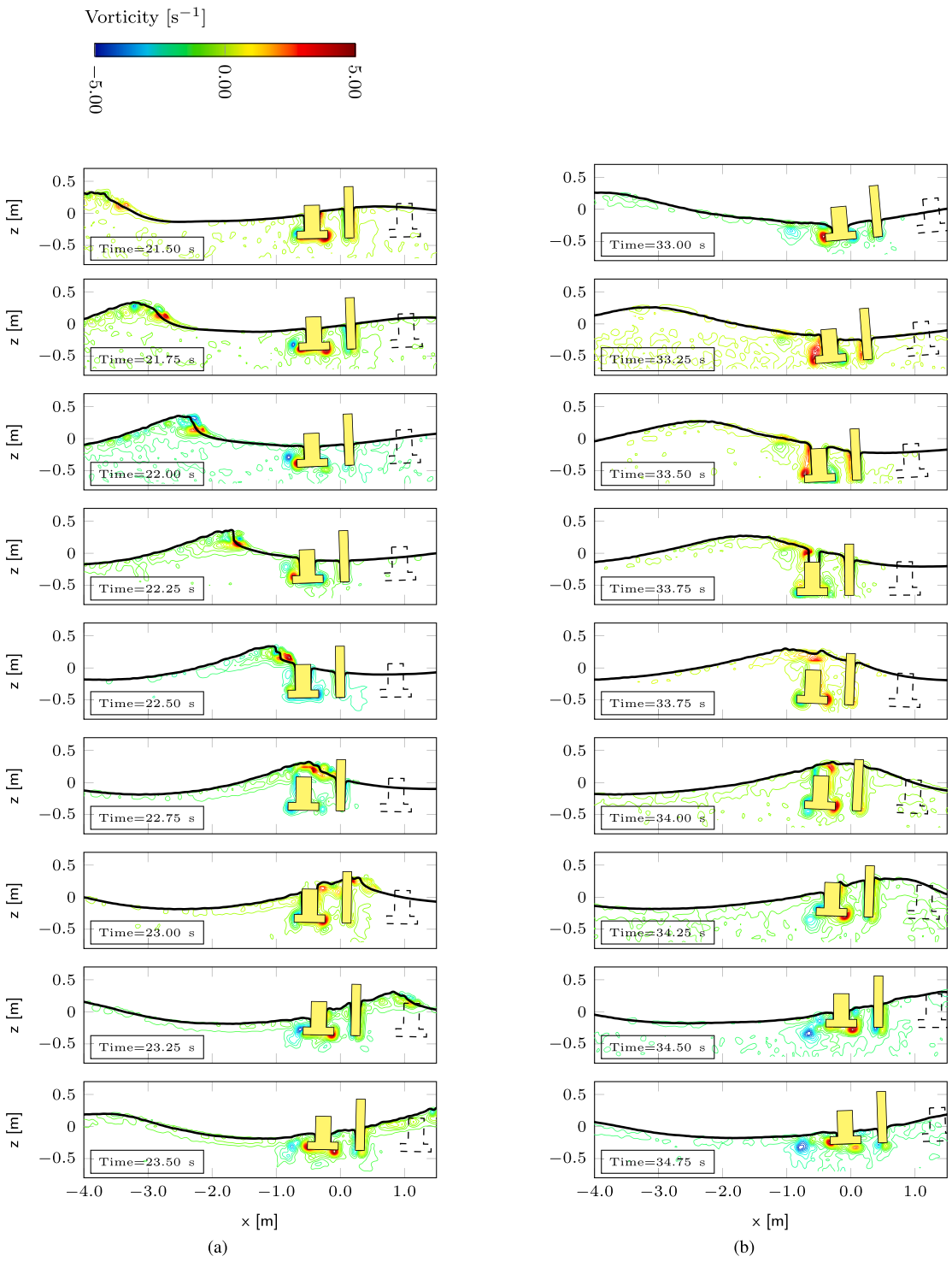

Fig. 17. Temporal sequences of y-component vorticity field covering the main crest impact with the DeepCwind platform for the Case *L* in **F1** (a) and **F2** (b). The solid black line indicates the free surface.

regular and irregular wave representations. Moreover, when comparing spectral data, the model successfully captured the most decisive components that contribute to the whole spectrum. However, high frequency force terms are underestimated possibly due to some lack of capability of the considered wave flume in generating and propagating those components. Sensitivity analysis of the model resolution has provided clear insights into the relatively low level of resolution required to predict wave-induced loads with high accuracy, giving consistent results in terms of the propagated spectral components.

Lastly, an innovative, incremental focused wave investigation has proposed technically relevant information for the ultimate limit state safety checks to be performed for semi-submersible platforms, providing agreement with the outcomes of other research on WECs and floating platforms. By investigating the response of the moored DeepCwind

platform when withstanding severe weather conditions represented via two ensembles of focused wave trains, either of them taken as the ideal bound of an environmental contour. Drawing on the data presented and discussed beforehand, we put forward the following conclusive remarks.

1. The wave steepness criterion alone may fail in identifying the most restrictive load case. This is very specific for this case due to the heave resonance period of the platform.
2. Waves with spectral characteristics that approach the heave resonance period produce higher tensions in the mooring systems, coupled to the large displacements in heave and surge that the platform experiences.
3. The maximum total horizontal and vertical forces are decoupled from the displacement peaks. An average reduction of 30% of the fluid-induced loads on the hull is observed.
4. Wave overtopping likelihood (and ensuing slamming loads) is maximized by very steep waves. The computations have revealed locally induced over pressure on the free-board of up to 100% higher than the expected for similar wave heights with a milder profile.

These conclusions directly affect the choice of the cases from environmental contours that often associate events to the pairing return period. The results in this work indicate that the most challenging scenarios can be triggered by wave frequencies that are capable of approaching the heave fundamental period. Once selected the wave conditions, the most energetic part spanning over a few wave periods should be checked in a continuous fashion (e.g., performing resistance or stability checks every one tenth of a period). This may spare the designer from combining loads (for example max tensions and max fluid loads) for which the likelihood of occurring simultaneously is extremely small.

Our work highlights some limitations of the SPH implementation used for this research. In particular, the formulation based on weakly compressible fluids may be the cause of high-frequency pressure noise in the pattern of the vertical force validation provided in the validation phase. Future iterations of the code could benefit from innovative formulations aimed at mitigating the limitations of WCSPH by addressing the continuity equation (Khayyer et al., 2023; Sun et al., 2023; Michel et al., 2023). The results of the decay tests suggest that new numerical advancements are needed to increase the applicability of the method to approach structures very sensitive to self-induced motions, and where viscosity and turbulence models may potentially be critical to achieving the required level of fidelity. Nevertheless, the proposed validated setup may provide a functional spring-board for boosting the performance investigation on FOWTs using the SPH. As of now, viscosity and turbulence configure still fields under investigation within the SPH community as remarked in Vacondio et al. (2020). The code that is distributed under the name DualSPHysics would hypothetically be able to tackle the hydroelastic analysis of the various components of the platform hull (O'Connor and Rogers, 2021) or address the dynamic behavior of the wind towers and rotor blades (Capasso et al., 2022; Martínez-Estévez et al., 2023b), whereas more detailed hydrodynamic investigations would be possible via the implementation of more comprehensive environmental loads, such as waves and currents (Capasso et al., 2023; Yang et al., 2023).

CRediT authorship contribution statement

Bonaventura Tagliafierro: Conceptualization, Validation, Investigation, Methodology, Formal analysis, Data curation, Visualization, Writing – original draft. **Madjid Karimirad:** Conceptualization, Investigation, Methodology, Data curation, Writing – review & editing, Supervision, Resources, Funding acquisition. **Corrado Altomare:** Supervision, Writing – review & editing, Resources, Funding acquisition. **Malin Göteman:** Supervision, Writing – review & editing, Resources, Funding acquisition. **Iván Martínez-Estévez:** Software, Resources, Writing – review & editing. **Salvatore Capasso:** Conceptualization, Validation, Investigation, Methodology, Formal analysis, Data curation, Visualization, Writing – review & editing. **José M. Domínguez:** Software, Resources, Writing – review & editing. **Giacomo Viccione:** Supervision, Writing – review & editing, Project administration, Resources, Funding acquisition. **Moncho Gómez-Gesteira:** Supervision, Writing – review & editing, Project administration, Resources, Funding acquisition. **Alejandro J.C. Crespo:** Conceptualization, Validation, Visualization, Methodology, Investigation, Writing – original draft, Supervision, Resources, Funding acquisition.

Declaration of competing interest

The authors wish to confirm that there are no known conflicts of interest associated with this publication and there has been no significant financial support for this work that could have influenced its outcome. We confirm that the manuscript has been read and approved by all named authors and that there are no other persons who satisfied the criteria for authorship but are not listed. We further confirm that the order of authors listed in the manuscript has been approved by all of us. We confirm that we have given due consideration to the protection of intellectual property associated with this work and that there are no impediments to publication, including the timing of publication, with respect to intellectual property. In so doing we confirm that we have followed the regulations of our institutions concerning intellectual property.

Data availability

We attached a database that contains the data we want to share.

Acknowledgments

Funding for open access charge: Universidade de Vigo/CISUG. We are grateful for the use of the computing resources from the Northern Ireland High Performance Computing (NI-HPC) service funded by EPSRC, UK (EP/T022175). M. Göteman and B. Tagliafierro acknowledge the support provided by the National Academic Infrastructure for Super-computing in Sweden (NAISS) through the project 2022-5-649 for the use of the GPU partition Tetralith2 at the National Supercomputer Centre (NSC). This work was partially supported by the project SURVIWEC PID2020-113245RB-I00 financed by MCIN/AEI/10.13039/501100011033 and by the project ED431C 2021/44 "Programa de Consolidación e Estructuración de Unidades de Investigación Competitivas" financed by Xunta de Galicia, Consellería de Cultura, Educación e Universidade, Spain. Grant TED2021-129479A-I00 funded by Ministerio de Ciencia e Innovacion, Spain (MCIN/AEI/10.13039/501100011033) and by the "European Union NextGenerationEU/PRTR".

Funding for open access charge: Universidade de Vigo/CISUGB. Tagliafierro expresses gratitude for the scientific support provided by the Project Chrono team, led by Prof. Dan Negrut (UW-Madison) and Dr. Radu Serban (UW-Madison). B. Tagliafierro gratefully acknowledges financial support for this publication by the Fulbright Schuman Program, which is administered by the Fulbright Commission in Brussels and jointly financed by the U.S. Department of State, and the Directorate-General for Education, Youth, Sport and Culture (DG.EAC) of the European Commission. Its contents are solely the responsibility of the author and do not necessarily represent the official views of the Fulbright Program, the Government of the United States, or the Fulbright Commission in Brussels. Dr. Corrado Altomare acknowledges funding from the Spanish government and the European Social Found (ESF) under the programme 'Ramón *y* Cajal 2020' (RYC2020-030197-I/AEI/10.13039/501100011033) and within the project GLORIA PID2020-115030RJ-I00 "Adquirir conocimientos sobre el riesgo de rebase para las zonas costeras urbanizadas" (MCIN/AEI/10.13039/

501100011033). I. Martínez-Estévez acknowledges funding from Xunta de Galicia, Spain under "Programa de axudas á etapa predoutoral da Consellería de Cultura, Educación e Universidades da Xunta de Galicia" (ED481A-2021/337).

Appendix A. Data conversion for the experimental dataset

The experimental reference data used for this work is available at A2e Data Archive and Portal and A2e Data Archive and Portal. The information presented in this manuscript pertains to the model scale, so no scaling procedures were necessary to compare physical and numerical models. However, the reference datasets utilized data that was manipulated using Froude's similitude scale laws to make reference to the prototype geometry. To retrieve the experimental values, an inverse procedure was applied. Specifically, for geometry-related parameters (such as distances) and time, the scaling factor corresponds solely to the Froude scaling factor, as described in Giannini et al. (2020). For pressure, force, and mass, an additional term was included to account for the water density change. As a matter of fact, the datasets were projected towards sea water (salted) with a hypothetical density of 1025 kg/m^3. More specifically, a generic quantity at the model scale $(\cdot)_m$ was transformed using the following equation:

$$(\cdot)_m = \lambda^x \frac{\rho_m}{\rho_p}(\cdot)_p \tag{A.1}$$

where λ^x represents the geometric scaling ratio (which is 50 in this case; x matches 1 for pressure, 3 for forces, and 3 for mass) ρ_m and ρ_p are the densities of water at the model scale and full scale, respectively, and $(\cdot)_p$ indicates the variable given at full scale.

Appendix B. Data reproducibility

The parameters given in Section 5.1 may be used to reconstruct the piston motion using a numerical model based on the theory described in , for all the wave conditions reported in Tables 8 and 9. However, the piston stroke information for the generation of the focused wave listed in the manuscript is shared using an external repository that can be found at the following link GitHub-repository (Tagliafierro et al., 2023b). The repository comprises two folders in which the files are named according to the case they refer to using the nomenclature in the reference tables. Each file has three columns: time (in seconds), paddle position (in meters), and the target surface elevation at the focusing position (in meters).

The dataset is distributed using the GPL-3.0 license, and its terms of use are given in a LICENSE file embedded into the repository.

Appendix C. Supplementary data

Supplementary material related to this article can be found online at https://doi.org/10.1016/j.apor.2023.103757.

References

A2e Data Archive and Portal, Atmosphere to Electrons (A2e). U.S. Department of Energy, Office of Energy Efficiency and Renewable Energy, http://dx.doi.org/10.21947/1775070, https://a2e.energy.gov/. (Accessed 16 April 2023).

A2e Data Archive and Portal, 2023. Atmosphere to Electrons (A2e). U.S. Department of Energy, Office of Energy Efficiency and Renewable Energy, http://dx.doi.org/10.21947/1959725, https://a2e.energy.gov/. (Accessed 16 April 2023).

Altomare, C., Domínguez, J., Crespo, A., González-Cao, J., Suzuki, T., Gómez-Gesteira, M., Troch, P., 2017. Long-crested wave generation and absorption for SPH-based DualSPHysics model. Coast. Eng. 127, 37–54. http://dx.doi.org/10.1016/j.coastaleng.2017.06.004.

Altomare, C., Domínguez, J.M., Crespo, A.J.C., Suzuki, T., Caceres, I., Gómez-Gesteira, M., 2015. Hybridization of the wave propagation model SWASH and the meshfree particle method SPH for real coastal applications. Coast. Eng. J. 57 (4), 1550024–1–1550024–34. http://dx.doi.org/10.1142/S0578563415500242, Publisher: Taylor & Francis _eprint.

Altomare, C., Domínguez, J.M., Fourtakas, G., 2022. Latest developments and application of SPH using DualSPHysics. Comput. Part. Mech. 9 (5), 863–866. http://dx.doi.org/10.1007/s40571-022-00499-1, URL: https://www.scopus.com/inward/record.uri?eid=2-s2.0-85134598000&doi=10.1007%2fs40571-022-00499-1&partnerID=40&md5=ed5a8f48d5a729dfc552cf15aad9d20f.

Altomare, C., Gironella, X., Crespo, A.J., 2021. Simulation of random wave overtopping by a WCSPH model. Appl. Ocean Res. 116, http://dx.doi.org/10.1016/j.apor.2021.102888, URL: https://www.scopus.com/inward/record.uri?eid=2-s2.0-85115771077&doi=10.1016%2fj.apor.2021.102888&partnerID=40&md5=496619ecdc55e1b21c653caecf03b656.

Altomare, C., Tagliafierro, B., Dominguez, J.M., Suzuki, T., Viccione, G., 2018. Improved relaxation zone method in SPH-based model for coastal engineering applications. Appl. Ocean Res. 81, 15–33. http://dx.doi.org/10.1016/j.apor.2018.09.013, URL: https://www.sciencedirect.com/science/article/pii/S0141118718303705.

Amicarelli, A., Manenti, S., Albano, R., Agate, G., Paggi, M., Longoni, L., Mirauda, D., Ziane, L., Viccione, G., Todeschini, S., Sole, A., Baldini, L., Brambilla, D., Papini, M., Khellaf, M., Tagliafierro, B., Sarno, L., Pirovano, G., 2020. SPHERA v.9.0.0: A Computational Fluid Dynamics research code, based on the Smoothed Particle Hydrodynamics mesh-less method. Comput. Phys. Comm. 250, http://dx.doi.org/10.1016/j.cpc.2020.107157.

Anon, 2009. DNV-RP-F205: Global Performance Analysis of Deepwater Floating Structures. Technical Report.

Antuono, M., Colagrossi, A., Marrone, S., 2012. Numerical diffusive terms in weakly-compressible SPH schemes. Comput. Phys. Comm. 183 (12), 2570–2580. http://dx.doi.org/10.1016/j.cpc.2012.07.006, URL: http://www.sciencedirect.com/science/article/pii/S0010465512002342.

Asim, T., Islam, S.Z., Hemmati, A., Khalid, M.S.U., 2022. A review of recent advancements in offshore wind turbine technology. Energies 15 (2), http://dx.doi.org/10.3390/en15020579, URL: https://www.mdpi.com/1996-1073/15/2/579.

Bandringa, H., Helder, J.A., 2018. On the validity and sensitivity of CFD simulations for a deterministic breaking wave impact on a semi submersible. In: International Conference on Offshore Mechanics and Arctic Engineering, Volume 1: Offshore Technology, http://dx.doi.org/10.1115/OMAE2018-78089, V001T01A004.

Bihs, H., Wang, W., Pakozdi, C., Kamath, A., 2020. REEF3D::FNPF—A flexible fully nonlinear potential flow solver. J. Offshore Mech. Arct. Eng. 142 (4), http://dx.doi.org/10.1115/1.4045915, 041902.

Blin, L., Hadjadj, A., Vervisch, L., 2003. Large eddy simulation of turbulent flows in reversing systems. J. Turbulence 4, http://dx.doi.org/10.1088/1468-5248/4/1/001.

Brito, M., Canelas, R., García-Feal, O., Domínguez, J., Crespo, A., Ferreira, R., Neves, M., Teixeira, L., 2020. A numerical tool for modelling oscillating wave surge converter with nonlinear mechanical constraints. Renew. Energy 146, 2024–2043. http://dx.doi.org/10.1016/j.renene.2019.08.034.

Butterfield, S., Musial, W., Jonkman, J., Sclavounos, P., 2007. Engineering challenges for floating offshore wind turbines. In: Presented At the 2005 Copenhagen Offshore Wind Conference, 26-28 October 2005, Copenhagen, Denmark. National Renewable Energy Laboratory, Golden, CO, United States, URL: https://www.osti.gov/biblio/917212. Report Number: NREL/CP-500-38776.

Canelas, R.B., Domínguez, J.M., Crespo, A.J., Gómez-Gesteira, M., Ferreira, R.M., 2015. A Smooth Particle Hydrodynamics discretization for the modelling of free surface flows and rigid body dynamics. Internat. J. Numer. Methods Fluids 78 (9), 581–593. http://dx.doi.org/10.1002/fld.4031.

Capasso, S., Tagliafierro, B., Güzel, H., Yilmaz, A., Dal, K., Kocaman, S., Viccione, G., Evangelista, S., 2021. A numerical validation of 3D experimental dam-break wave interaction with a sharp obstacle using DualSPHysics. Water 13 (15), http://dx.doi.org/10.3390/w13152133.

Capasso, S., Tagliafierro, B., Mancini, S., Martínez-Estévez, I., Altomare, C., Domínguez, J.M., Viccione, G., 2023. Regular wave seakeeping analysis of a planing hull by smoothed particle hydrodynamics: A comprehensive validation. J. Mar. Sci. Eng. 11 (4), http://dx.doi.org/10.3390/jmse11040700, URL: https://www.mdpi.com/2077-1312/11/4/700.

Capasso, S., Tagliafierro, B., Martínez-Estévez, I., Domínguez, J., Crespo, A., Viccione, G., 2022. A DEM approach for simulating flexible beam elements with the Project Chrono core module in DualSPHysics. Comput. Part. Mech. http://dx.doi.org/10.1007/s40571-021-00451-9, URL: https://www.scopus.com/inward/record.uri?eid=2-s2.0-85123868462&doi=10.1007%2fs40571-021-00451-9&partnerID=40&md5=bfcb576331b5c69d91c0688feea939d6.

Chen, Y.-H., Yang, R.-Y., 2021. Study on array floating platform for wind energy and marine space optimization. Sustainability 13 (24), http://dx.doi.org/10.3390/su132414014, URL: https://www.mdpi.com/2071-1050/13/24/14014.

Chow, A.D., Stansby, P.K., Rogers, B.D., Lind, S.J., Fang, Q., 2022. Focused wave interaction with a partially-immersed rectangular box using 2-D incompressible SPH on a GPU comparing with experiment and linear theory. Eur. J. Mech. B/Fluids http://dx.doi.org/10.1016/j.euromechflu.2022.05.007, URL: https://www.sciencedirect.com/science/article/pii/S0997754622000802.

Clauss, G.F., Bergmann, J., 1986. Gaussian wave packets — A new approach to seakeeping testsof ocean structures. Appl. Ocean Res. 8 (4), 190–206. http://dx.doi.org/10.1016/S0141-1187(86)80036-0, URL: https://www.sciencedirect.com/science/article/pii/S0141118786800360.

Crespo, A., Altomare, C., Domínguez, J., González-Cao, J., Gómez-Gesteira, M., 2017. Towards simulating floating offshore oscillating water column converters with Smoothed Particle Hydrodynamics. Coast. Eng. 126, 11–26. http://dx.doi.org/10.1016/j.coastaleng.2017.05.001.

Dagher, H., Viselli, A., Goupee, A., Allen, C., 2017. 1:50 scale testing of three floating wind turbines at MARIN and numerical model validation against test data. http://dx.doi.org/10.2172/1375021, URL: https://www.osti.gov/biblio/1375021.

Dalrymple, R.A., Rogers, B., 2006. Numerical modeling of water waves with the SPH method. Coast. Eng. 53 (2–3), 141–147. http://dx.doi.org/10.1016/j.coastaleng.2005.10.004, URL: https://www.scopus.com/inward/record.uri?eid=2-s2.0-32044462765&doi=10.1016%2fj.coastaleng.2005.10.004&partnerID=40&md5=d61cc4abef015ecb7df985c1fc5c656c. Cited by: 580.

Davidson, J., Costello, R., 2020. Efficient nonlinear hydrodynamic models for wave energy converter design—A scoping study. J. Mar. Sci. Eng. 8 (1), http://dx.doi.org/10.3390/jmse8010035, URL: https://www.mdpi.com/2077-1312/8/1/35.

Davidson, J., Giorgi, S., Ringwood, J.V., 2015. Linear parametric hydrodynamic models for ocean wave energy converters identified from numerical wave tank experiments. Ocean Eng. 103, 31–39. http://dx.doi.org/10.1016/j.oceaneng.2015.04.056, URL: https://www.sciencedirect.com/science/article/pii/S0029801815001432.

Dean, R., Dalrymple, R., 1984. Water Wave Mechanics for Engineers and Scientists. Prentice-Hall Inc, URL: https://www.scopus.com/inward/record.uri?eid=2-s2.0-85040805103&partnerID=40&md5=026245f13b3d10cae61124d20aa26b8e.

DNV-ST-0119, 2016. Loads and Site Conditions for Wind Turbines. Det Norske Veritas, DNV: Oslo, Norway.

DNV-ST-0119, 2021. Floating Wind Turbine Structures. Technical Report, Det Norske Veritas, DNV: Oslo, Norway.

Domínguez, J.M., Altomare, C., Gonzalez-Cao, J., Lomonaco, P., 2019a. Towards a more complete tool for coastal engineering: Solitary wave generation, propagation and breaking in an SPH-based model. Coast. Eng. J. 61 (1), 15–40. http://dx.doi.org/10.1080/21664250.2018.1560682, Publisher: Taylor & Francis _eprint.

Domínguez, J., Crespo, A., Hall, M., Altomare, C., Wu, M., Stratigaki, V., Troch, P., Cappietti, L., Gómez-Gesteira, M., 2019b. SPH simulation of floating structures with moorings. Coast. Eng. 153, 103560. http://dx.doi.org/10.1016/j.coastaleng.2019.103560.

Domínguez, J.M., Fourtakas, G., Altomare, C., Canelas, R.B., Tafuni, A., García-Feal, O., Martínez-Estévez, I., Mokos, A., Vacondio, R., Crespo, A.J.C., Rogers, B.D., Stansby, P.K., Gómez-Gesteira, M., 2022. DualSPHysics: From fluid dynamics to multiphysics problems. Comput. Part. Mech. 9 (5), 867–895. http://dx.doi.org/10.1007/s40571-021-00404-2.

English, A., Domínguez, J., Vacondio, R., Crespo, A., Stansby, P., Lind, S., Chiapponi, L., Gómez-Gesteira, M., 2022. Modified dynamic boundary conditions (mDBC) for general-purpose smoothed particle hydrodynamics (SPH): application to tank sloshing, dam break and fish pass problems. Comput. Part. Mech. 9 (5), 1–15. http://dx.doi.org/10.1007/s40571-021-00403-3, URL: https://www.scopus.com/inward/record.uri?eid=2-s2.0-85103385297&doi=10.1007%2fs40571-021-00403-3&partnerID=40&md5=9c42490a240326320537466675df4c27.

Fang, X., Guo, X., Tian, X., Wang, P., Lu, W., Li, X., 2023. A review on the numerical and experimental modeling of the floatover installations. Ocean Eng. 272, 113774. http://dx.doi.org/10.1016/j.oceaneng.2023.113774, URL: https://www.sciencedirect.com/science/article/pii/S0029801823001580.

Fourtakas, G., Dominguez, J.M., Vacondio, R., Rogers, B.D., 2019. Local uniform stencil (LUST) boundary condition for arbitrary 3-D boundaries in parallel smoothed particle hydrodynamics (SPH) models. Comput. & Fluids 190, 346–361. http://dx.doi.org/10.1016/j.compfluid.2019.06.009.

Fowler, M.J., Goupee, A.J., Allen, C., Viselli, A., Dagher, H., 2017. 1:52 scale testing of the first US commercial scale floating wind turbine, VolturnUS: Testing overview and the evolution of scale model testing methods. In: International Conference on Offshore Mechanics and Arctic Engineering, Volume 10: Ocean Renewable Energy, http://dx.doi.org/10.1115/OMAE2017-61864, V010T09A078.

Fries, T.-P., Matthies, H.G., 2006. A stabilized and coupled meshfree/meshbased method for the incompressible Navier-Stokes equations—Part II: Coupling. Comput. Methods Appl. Mech. Engrg. 195 (44), 6191–6204. http://dx.doi.org/10.1016/j.cma.2005.12.003, URL: https://www.sciencedirect.com/science/article/pii/S0045782506000181.

Giannini, G., Temiz, I., Rosa-Santos, P., roozi, Z., Ramos, V., Göteman, M., Engström, J., Day, S., Taveira-Pinto, F., 2020. Wave energy converter power take-off system scaling and physical modelling. J. Mar. Sci. Eng. 8 (9), http://dx.doi.org/10.3390/jmse8090632, URL: https://www.mdpi.com/2077-1312/8/9/632.

Gomez-Gesteira, M., Rogers, B., Crespo, A., Dalrymple, R., Narayanaswamy, M., Dominguez, J., 2012. SPHysics - development of a free-surface fluid solver - Part 1: Theory and formulations. Comput. Geosci. 48, 289–299. http://dx.doi.org/10.1016/j.cageo.2012.02.029.

Göteman, M., Engström, J., Eriksson, M., Hann, M., Ransley, E., Greaves, D., Leijon, M., 2015. Wave loads on a point-absorbing wave energy device in extreme waves. In: International Ocean and Polar Engineering Conference, All Days. ISOPE-I-15-593.

Gotoh, H., Khayyer, A., 2018. On the state-of-the-art of particle methods for coastal and ocean engineering. Coast. Eng. J. 60 (1), 79–103. http://dx.doi.org/10.1080/21664250.2018.1436243.

Gotoh, H., Khayyer, A., Shimizu, Y., 2021. Entirely Lagrangian meshfree computational methods for hydroelastic fluid-structure interactions in ocean engineering—Reliability, adaptivity and generality. Appl. Ocean Res. 115, 102822. http://dx.doi.org/10.1016/j.apor.2021.102822, URL: https://www.sciencedirect.com/science/article/pii/S0141118721002959.

Harlow, F.H., 2004. Fluid dynamics in Group T-3 Los Alamos National Laboratory. Zenodo, http://dx.doi.org/10.1016/j.jcp.2003.09.031.

Hasselmann, K., Barnett, T., Bouws, E., Carlson, H., Cartwright, D., Enke, K., Ewing, J., Gienapp, H., Hasselmann, D., Kruseman, P., Meerburg, A., Muller, P., Olbers, D., Richter, K., Sell, W., Walden, H., 1973. Measurements of wind-wave growth and swell decay during the Joint North Sea Wave Project (JONSWAP). Deut. Hydrogr. Z. 8, 1–95.

Huang, L., Li, Y., Benites-Munoz, D., Windt, C.W., Feichtner, A., Tavakoli, S., Davidson, J., Paredes, R., Quintuna, T., Ransley, E., Colombo, M., Li, M., Cardiff, P., Tabor, G., 2022. A review on the modelling of wave-structure interactions based on OpenFOAM. OpenFOAM® J. 2, 116–142. http://dx.doi.org/10.51560/ofj.v2.65.

IEA, 2022. Wind Electricity. Technical Report, IEA, Paris, URL: https://www.iea.org/reports/wind-electricity. License: CC BY 4.0.

Jiang, Z., 2021. Installation of offshore wind turbines: A technical review. Renew. Sustain. Energy Rev. 139, 110576. http://dx.doi.org/10.1016/j.rser.2020.110576, URL: https://www.sciencedirect.com/science/article/pii/S1364032120308601.

Jonkman, J.M., 2007. Dynamics modeling and loads analysis of an offshore floating wind turbine (Ph.D. thesis). p. 328, URL: https://ezproxy.library.wisc.edu/login?url=https://www.proquest.com/dissertations-theses/dynamics-modeling-loads-analysis-offshore/docview/304888850/se-2. Copyright - Database copyright ProQuest LLC; ProQuest does not claim copyright in the individual underlying works; Last updated - 2023-02-24,

Karimirad, M., Moan, T., 2012. Wave- and wind-induced dynamic response of a spar-type offshore wind turbine. J. Waterw. Port Coast. Ocean Eng. 138 (1), 9–20. http://dx.doi.org/10.1061/(ASCE)WW.1943-5460.0000087, arXiv:https://ascelibrary.org/doi/pdf/10.1061/%28ASCE%29WW.1943-5460.0000087. URL: https://ascelibrary.org/doi/abs/10.1061/%28ASCE%29WW.1943-5460.0000087.

Katsidoniotaki, E., Göteman, M., 2022. Numerical modeling of extreme wave interaction with point-absorber using OpenFOAM. Ocean Eng. 245, 110268. http://dx.doi.org/10.1016/j.oceaneng.2021.110268, URL: https://www.sciencedirect.com/science/article/pii/S0029801821015754.

Katsidoniotaki, E., Nilsson, E., Rutgersson, A., Engström, J., Göteman, M., 2021. Response of point-absorbing wave energy conversion system in 50-years return period extreme focused waves. J. Mar. Sci. Eng. 9 (3), http://dx.doi.org/10.3390/jmse9030345, URL: https://www.mdpi.com/2077-1312/9/3/345.

Katsidoniotaki, E., Shahroozi, Z., Eskilsson, C., Palm, J., Engström, J., Göteman, M., 2023. Validation of a CFD model for wave energy system dynamics in extreme waves. Ocean Eng. 268, 113320. http://dx.doi.org/10.1016/j.oceaneng.2022.113320, URL: https://www.sciencedirect.com/science/article/pii/S0029801822026038.

Khayyer, A., Shimizu, Y., Gotoh, T., Gotoh, H., 2023. Enhanced resolution of the continuity equation in explicit weakly compressible SPH simulations of incompressible free-surface fluid flows. Appl. Math. Model. 116, 84–121. http://dx.doi.org/10.1016/j.apm.2022.10.037, URL: https://www.sciencedirect.com/science/article/pii/S0307904X22005091.

Kvittem, M.I., Bachynski, E.E., Moan, T., 2012. Effects of hydrodynamic modelling in fully coupled simulations of a semi-submersible wind turbine. Energy Procedia 24, 351–362. http://dx.doi.org/10.1016/j.egypro.2012.06.118, URL: https://www.sciencedirect.com/science/article/pii/S1876610212011587. Selected papers from Deep Sea Offshore Wind R&D Conference, Trondheim, Norway, 19-20 January 2012.

Leble, V., Barakos, G., 2016a. A coupled floating offshore wind turbine analysis with high-fidelity methods. Energy Procedia 94, 523–530. http://dx.doi.org/10.1016/j.egypro.2016.09.229, URL: https://www.sciencedirect.com/science/article/pii/S1876610216309158. 13th Deep Sea Offshore Wind R&D Conference, EERA DeepWind'2016.

Leble, V., Barakos, G., 2016b. Demonstration of a coupled floating offshore wind turbine analysis with high-fidelity methods. J. Fluids Struct. 62, 272–293. http://dx.doi.org/10.1016/j.jfluidstructs.2016.02.001, URL: https://www.sciencedirect.com/science/article/pii/S088997461600027X.

Leimkuhler, B., Reich, S., Zentrum, K., Str, H., Skeel, R., 1995. Integration Methods for Molecular Dynamics. Vol. 82. http://dx.doi.org/10.1007/978-1-4612-4066-2_10.

Li, H., Bachynski-Polić, E.E., 2021. Experimental and numerically obtained low-frequency radiation characteristics of the OC5-DeepCwind semisubmersible. Ocean Eng. 232, 109130. http://dx.doi.org/10.1016/j.oceaneng.2021.109130, URL: https://www.sciencedirect.com/science/article/pii/S0029801821005655.

Liu, G., Liu, M., 2003. Smoothed Particle Hydrodynamics. WORLD SCIENTIFIC, http://dx.doi.org/10.1142/5340.

Liu, M., Liu, G., 2006. Restoring particle consistency in smoothed particle hydrodynamics. Appl. Numer. Math. 56 (1), 19–36. http://dx.doi.org/10.1016/j.apnum.2005.02.012, URL: https://www.sciencedirect.com/science/article/pii/S0168927405000565.

Liu, Y., Xiao, Q., Incecik, A., Peyrard, C., Wan, D., 2017. Establishing a fully coupled CFD analysis tool for floating offshore wind turbines. Renew. Energy 112, 280–301. http://dx.doi.org/10.1016/j.renene.2017.04.052, URL: https://www.sciencedirect.com/science/article/pii/S0960148117303609.

Lo, E.Y.M., Shao, S., 2002. Simulation of near-shore solitary wave mechanics by an incompressible SPH method. Appl. Ocean Res. 24 (5), 275–286. http://dx.doi.org/10.1016/S0141-1187(03)00002-6, URL: https://www.sciencedirect.com/science/article/pii/S0141118703000026.

Lopez-Pavon, C., Souto-Iglesias, A., 2015. Hydrodynamic coefficients and pressure loads on heave plates for semi-submersible floating offshore wind turbines: A comparative analysis using large scale models. Renew. Energy 81, 864–881. http://dx.doi.org/10.1016/j.renene.2015.04.003, URL: https://www.sciencedirect.com/science/article/pii/S0960148115002839.

Luo, M., Khayyer, A., Lin, P., 2021. Particle methods in ocean and coastal engineering. Appl. Ocean Res. 114, 102734. http://dx.doi.org/10.1016/j.apor.2021.102734, URL: https://www.sciencedirect.com/science/article/pii/S014111872100211X.

Madsen, O.S., 1971. On the generation of long waves. J. Geophys. Res. (1896-1977) 76 (36), 8672–8683. http://dx.doi.org/10.1029/JC076i036p08672, arXiv:https://agupubs.onlinelibrary.wiley.com/doi/pdf/10.1029/JC076i036p08672. URL: https://agupubs.onlinelibrary.wiley.com/doi/abs/10.1029/JC076i036p08672.

Martínez-Estévez, I., Domínguez, J.M., Tagliafierro, B., Canelas, R.B., García-Feal, O., Crespo, A.J.C., Gómez-Gesteira, M., 2023a. Coupling of an SPH-based solver with a multiphysics library. Comput. Phys. Comm. 283, 108581. http://dx.doi.org/10.1016/j.cpc.2022.108581, URL: https://www.sciencedirect.com/science/article/pii/S0010465522003009.

Martínez-Estévez, I., Tagliafierro, B., El Rahi, J., Domínguez, J., Crespo, A., Troch, P., Gómez-Gesteira, M., 2023b. Coupling an SPH-based solver with an FEA structural solver to simulate free surface flows interacting with flexible structures. Comput. Methods Appl. Mech. Engrg. 410, 115989. http://dx.doi.org/10.1016/j.cma.2023.115989, URL: https://www.sciencedirect.com/science/article/pii/S0045782523001123.

Masud, A., Hughes, T.J., 1997. A space-time Galerkin/least-squares finite element formulation of the Navier-Stokes equations for moving domain problems. Comput. Methods Appl. Mech. Engrg. 146 (1), 91–126. http://dx.doi.org/10.1016/S0045-7825(96)01222-4, URL: https://www.sciencedirect.com/science/article/pii/S0045782596012224.

Michel, J., Antuono, M., Oger, G., Marrone, S., 2023. Energy balance in quasi-Lagrangian Riemann-based SPH schemes. Comput. Methods Appl. Mech. Engrg. 410, 116015. http://dx.doi.org/10.1016/j.cma.2023.116015, URL: https://www.sciencedirect.com/science/article/pii/S0045782523001391.

Mitsui, J., Altomare, C., Crespo, A.J., Domínguez, J.M., Martínez-Estévez, I., Suzuki, T., ichi Kubota, S., Gómez-Gesteira, M., 2023. DualSPHysics modelling to analyse the response of Tetrapods against solitary wave. Coast. Eng. 183, 104315. http://dx.doi.org/10.1016/j.coastaleng.2023.104315, URL: https://www.sciencedirect.com/science/article/pii/S037838392300039X.

Molteni, D., Colagrossi, A., 2009. A simple procedure to improve the pressure evaluation in hydrodynamic context using the SPH. Comput. Phys. Comm. 180 (6), 861–872. http://dx.doi.org/10.1016/j.cpc.2008.12.004.

Monaghan, J.J., Cas, R.A.F., Kos, A.M., Hallworth, M., 1999. Gravity currents descending a ramp in a stratified tank. J. Fluid Mech. 379, 39–69. http://dx.doi.org/10.1017/S0022112098003280.

Monaghan, J.J., Kos, A., 1999. Solitary waves on a cretan beach. J. Waterw. Port Coast. Ocean Eng. 125 (3), 145–155. http://dx.doi.org/10.1061/(ASCE)0733-950X(1999)125:3(145), URL: https://ascelibrary.org/doi/abs/10.1061/%28ASCE%290733-950X%281999%29125%3A3%28145%29.

Monaghan, J., Kos, A., Issa, N., 2003. Fluid motion generated by impact. J. Waterw. Port Coast. Ocean Eng. 129 (6), 250–259. http://dx.doi.org/10.1061/(ASCE)0733-950X(2003)129:6(250).

Mortimer, W., Calvert, R., Antonini, A., Greaves, D., Raby, A., van den Bremer, T.S., 2023. Implications of second-order wave generation for physical modelling of force and run-up on a vertical wall using wave groups. Coast. Eng. 180, 104259. http://dx.doi.org/10.1016/j.coastaleng.2022.104259, URL: https://www.sciencedirect.com/science/article/pii/S0378383922001727.

Muliawan, M.J., Karimirad, M., Gao, Z., Moan, T., 2013. Extreme responses of a combined spar-type floating wind turbine and floating wave energy converter (STC) system with survival modes. Ocean Eng. 65, 71–82. http://dx.doi.org/10.1016/j.oceaneng.2013.03.002, URL: https://www.sciencedirect.com/science/article/pii/S002980181300111X.

Myhr, A., Bjerkseter, C., Ågotnes, A., Nygaard, T.A., 2014. Levelised cost of energy for offshore floating wind turbines in a life-cycle perspective. Renew. Energy 66, 714–728. http://dx.doi.org/10.1016/j.renene.2014.01.017, URL: https://www.sciencedirect.com/science/article/pii/S0960148114000469.

Nematbakhsh, A., Bachynski, E.E., Gao, Z., Moan, T., 2015. Comparison of wave load effects on a TLP wind turbine by using computational fluid dynamics and potential flow theory approaches. Appl. Ocean Res. 53, 142–154. http://dx.doi.org/10.1016/j.apor.2015.08.004, URL: https://www.sciencedirect.com/science/article/pii/S0141118715001108.

O'Connor, J., Rogers, B.D., 2021. A fluid–structure interaction model for free-surface flows and flexible structures using smoothed particle hydrodynamics on a GPU. J. Fluids Struct. 104, 103312. http://dx.doi.org/10.1016/j.jfluidstructs.2021.103312, URL: https://www.sciencedirect.com/science/article/pii/S0889974621000955.

Oger, G., Le Touzé, D., Ducrozet, G., Candelier, J., Guilcher, P.-M., 2014. A coupled sph-spectral method for the simulation of wave train impacts on a FPSO. In: Proceedings of the International Conference on Offshore Mechanics and Arctic Engineering - OMAE. Vol. 2. American Society of Mechanical Engineers (ASME), http://dx.doi.org/10.1115/OMAE2014-24679.

Oguz, E., Clelland, D., Day, A.H., Incecik, A., López, J.A., Sánchez, G., Almeria, G.G., 2018. Experimental and numerical analysis of a TLP floating offshore wind turbine. Ocean Eng. 147, 591–605. http://dx.doi.org/10.1016/j.oceaneng.2017.10.052, URL: https://www.sciencedirect.com/science/article/pii/S0029801817306649.

Opoku, F., Uddin, M., Atkinson, M., 2023. A review of computational methods for studying oscillating water columns – the Navier-Stokes based equation approach. Renew. Sustain. Energy Rev. 174, http://dx.doi.org/10.1016/j.rser.2022.113124, URL: https://www.scopus.com/inward/record.uri?eid=2-s2.0-85145216839&doi=10.1016%2fj.rser.2022.113124&partnerID=40&md5=f0ebc4585a96ff4ea73f35442c6efe1b. Cited by: 0.

Otter, A., Murphy, J., Pakrashi, V., Robertson, A., Desmond, C., 2022. A review of modelling techniques for floating offshore wind turbines. Wind Energy 25 (5), 831–857. http://dx.doi.org/10.1002/we.2701, arXiv:https://onlinelibrary.wiley.com/doi/pdf/10.1002/we.2701, URL: https://onlinelibrary.wiley.com/doi/abs/10.1002/we.2701.

Papalambros, P.Y., Wilde, D.J., 2017. Principles of Optimal Design: Modeling and Computation, third ed. Cambridge University Press, http://dx.doi.org/10.1017/9781316451038.

Pribadi, A., Donatini, L., Lataire, E., Verao Fernandez, G., Martínez-Estévez, I., 2023. Validation of a computationally efficient time-domain numerical tool against DeepCwind experimental data. In: C.G., S. (Ed.), Trends in Renewable Energies Offshore - Proceedings of the 5th International Conference on Renewable Energies Offshore, RENEW 2022. CRC Press/Balkema, pp. 597–608. http://dx.doi.org/10.1201/9781003360773-68.

Pringgana, G., Cunningham, L.S., Rogers, B.D., 2023. Mitigating tsunami effects on buildings via novel use of discrete onshore protection systems. Coast. Eng. J. 65 (1), 149–173. http://dx.doi.org/10.1080/21664250.2023.2170690.

Quartier, N., Crespo, A.J., Domínguez, J.M., Stratigaki, V., Troch, P., 2021. Efficient response of an onshore Oscillating Water Column Wave Energy Converter using a one-phase SPH model coupled with a multiphysics library. Appl. Ocean Res. 115, 102856. http://dx.doi.org/10.1016/j.apor.2021.102856, URL: https://www.sciencedirect.com/science/article/pii/S0141118721003278.

Rakhsha, M., Kees, C.E., Negrut, D., 2021. Lagrangian vs. Eulerian: An analysis of two solution methods for free-surface flows and fluid solid interaction problems. Fluids 6 (12), http://dx.doi.org/10.3390/fluids6120460, URL: https://www.mdpi.com/2311-5521/6/12/460.

Ransley, E., Greaves, D., Raby, A., Simmonds, D., Hann, M., 2017. Survivability of wave energy converters using CFD. Renew. Energy 109, 235–247. http://dx.doi.org/10.1016/j.renene.2017.03.003, URL: https://www.sciencedirect.com/science/article/pii/S0960148117301799.

Rehman, S., Alhems, L.M., Alam, M.M., Wang, L., Toor, Z., 2023. A review of energy extraction from wind and ocean: Technologies, merits, efficiencies, and cost. Ocean Eng. 267, 113192. http://dx.doi.org/10.1016/j.oceaneng.2022.113192, URL: https://www.sciencedirect.com/science/article/pii/S0029801822024751.

Roald, L., Jonkman, J., Robertson, A., Chokani, N., 2013. The effect of second-order hydrodynamics on floating offshore wind turbines. Energy Procedia 35, 253–264. http://dx.doi.org/10.1016/j.egypro.2013.07.178, URL: https://www.sciencedirect.com/science/article/pii/S1876610213012642. DeepWind'2013 – Selected papers from 10th Deep Sea Offshore Wind R&D Conference, Trondheim, Norway, 24 – 25 January 2013.

Robertson, A., Bachynski, E.E., Gueydon, S., Wendt, F., Schünemann, P., 2020a. Total experimental uncertainty in hydrodynamic testing of a semisubmersible wind turbine, considering numerical propagation of systematic uncertainty. Ocean Eng. 195, 106605. http://dx.doi.org/10.1016/j.oceaneng.2019.106605, URL: https://www.sciencedirect.com/science/article/pii/S0029801819307309.

Robertson, A.N., Gueydon, S., Bachynski, E., Wang, L., Jonkman, J., Alarcón, D., Amet, E., Beardsell, A., Bonnet, P., Boudet, B., Brun, C., Chen, Z., Féron, M., Forbush, D., Galinos, C., Galvan, J., Gilbert, P., Gómez, J., Harnois, V., Haudin, F., Hu, Z., Dreff, J.L., Leimeister, M., Lemmer, F., Li, H., Mckinnon, G., Mendikoa, I., Moghtadaei, A., Netzband, S., Oh, S., Pegalajar-Jurado, A., Nguyen, M.Q., Ruehl, K., Schünemann, P., Shi, W., Shin, H., Si, Y., Surmont, F., Trubat, P., Qwist, J., Wohlfahrt-Laymann, S., 2020b. OC6 Phase I: Investigating the underprediction of low-frequency hydrodynamic loads and responses of a floating wind turbine. J. Phys. Conf. Ser. 1618 (3), 032033. http://dx.doi.org/10.1088/1742-6596/1618/3/032033.

Robertson, A., Jonkman, J., Masciola, M., Song, H., Goupee, A., Coulling, A., Luan, C., 2014. Definition of the semisubmersible floating system for phase II of OC4. http://dx.doi.org/10.2172/1155123, URL: https://www.osti.gov/biblio/1155123.

Robertson, A., Wang, L., 2021. OC6 phase Ib: Floating wind component experiment for difference-frequency hydrodynamic load validation. Energies 14 (19), http://dx.doi.org/10.3390/en14196417, URL: https://www.mdpi.com/1996-1073/14/19/6417.

Robertson, A.N., Wendt, F., Jonkman, J.M., Popko, W., Dagher, H., Gueydon, S., Qvist, J., Vittori, F., Azcona, J., Uzunoglu, E., Soares, C.G., Harries, R., Yde, A., Galinos, C., Hermans, K., de Vaal, J.B., Bozonnet, P., Bouy, L., Bayati, I., Bergua, R., Galvan, J., Mendikoa, I., Sanchez, C.B., Shin, H., Oh, S., Molins, C., Debruyne, Y., 2017. OC5 project phase II: Validation of global loads of the DeepCwind floating semisubmersible wind turbine. Energy Procedia 137, 38–57. http://dx.doi.org/10.1016/j.egypro.2017.10.333, URL: https://www.sciencedirect.com/science/article/

pii/S1876610217352931. 14th Deep Sea Offshore Wind R&D Conference, EERA DeepWind'2017.

Ropero-Giralda, P., Crespo, A.J., Tagliafierro, B., Altomare, C., Domínguez, J.M., Gómez-Gesteira, M., Viccione, G., 2020. Efficiency and survivability analysis of a point-absorber wave energy converter using DualSPHysics. Renew. Energy 162, 1763–1776. http://dx.doi.org/10.1016/j.renene.2020.10.012, URL: http://www.sciencedirect.com/science/article/pii/S0960148120315780.

Schäffer, H.A., 1996. Second-order wavemaker theory for irregular waves. Ocean Eng. 23 (1), 47–88. http://dx.doi.org/10.1016/0029-8018(95)00013-B, URL: https://www.sciencedirect.com/science/article/pii/002980189500013B.

Shahroozi, Z., Göteman, M., Engström, J., 2022. Experimental investigation of a point-absorber wave energy converter response in different wave-type representations of extreme sea states. Ocean Eng. 248, 110693. http://dx.doi.org/10.1016/j.oceaneng.2022.110693, URL: https://www.sciencedirect.com/science/article/pii/S0029801822001482.

Shi, W., Zhang, L., Karimirad, M., Michailides, C., Jiang, Z., Li, X., 2023. Combined effects of aerodynamic and second-order hydrodynamic loads for floating wind turbines at different water depths. Appl. Ocean Res. 130, http://dx.doi.org/10.1016/j.apor.2022.103416, URL: https://www.scopus.com/inward/record.uri?eid=2-s2.0-85142524500&doi=10.1016%2fj.apor.2022.103416&partnerID=40&md5=3905fa85225db9f2d925a92ad8e10548.

Sjökvist, L., Wu, J., Ransley, E., Engström, J., Eriksson, M., Göteman, M., 2017. Numerical models for the motion and forces of point-absorbing wave energy converters in extreme waves. Ocean Eng. 145, 1–14. http://dx.doi.org/10.1016/j.oceaneng.2017.08.061, URL: https://www.sciencedirect.com/science/article/pii/S002980181730505X.

Smagorinsky, J., 1963. General circulation experiments with the primitive equations: I. the basic experiment. Mon. Weather Rev. 91 (3), 99–164. http://dx.doi.org/10.1175/1520-0493(1963)091<0099:GCEWTP>2.3.CO;2, URL: https://journals.ametsoc.org/view/journals/mwre/91/3/1520-0493_1963_091_0099_gcewtp_2_3_co_2.xml.

Sriram, V., Ma, Q., 2021. Review on the local weak form-based meshless method (MLPG): Developments and Applications in Ocean Engineering. Appl. Ocean Res. 116, 102883. http://dx.doi.org/10.1016/j.apor.2021.102883, URL: https://www.sciencedirect.com/science/article/pii/S0141118721003540.

Sun, P., Pilloton, C., Antuono, M., Colagrossi, A., 2023. Inclusion of an acoustic damper term in weakly-compressible SPH models. J. Comput. Phys. 483, 112056. http://dx.doi.org/10.1016/j.jcp.2023.112056, URL: https://www.sciencedirect.com/science/article/pii/S0021999123001511.

Suzuki, T., García-Feal, O., Domínguez, J.M., Altomare, C., 2022. Simulation of 3D overtopping flow–object–structure interaction with a calibration-based wave generation method with DualSPHysics and SWASH. Comput. Part. Mech. http://dx.doi.org/10.1007/s40571-022-00468-8, URL: https://www.scopus.com/inward/record.uri?eid=2-s2.0-85126228694&doi=10.1007%2fs40571-022-00468-8&partnerID=40&md5=628cef1294546869b94814a40627f928.

Tagliafierro, B., Göteman, M., Engström, J., Martí nez Estévez, I., Domínguez, J., Crespo, A., Gómez-Gesteira, M., Altomare, C., 2023a. Investigation into embedded focused wave group suitability for the assessment of extreme hydrodynamics loads on point-absorber WECs. pp. 421–430. http://dx.doi.org/10.1201/9781003360773-48.

Tagliafierro, B., Karimirad, M., Altomare, C., Göteman, M., Martínez-Estévez, I., Capasso, S., Domínguez, J.M., Viccione, G., Gómez-Gesteira, M., Crespo, A.J., 2023b. Numerical investigation of semi-submersible floating offshore wind turbine platforms interacting with focused wave trains: Dataset. GitHub repository, https://github.com/btagliafierro/APOR_dataset_2023. (Accessed 26 June 2023).

Tagliafierro, B., Karimirad, M., Martínez-Estévez, I., Domínguez, J., Crespo, A., Gómez-Gesteira, M., Viccione, G., 2022a. Preliminary Study Of Floating Offshore Wind Turbines Motions Using The Smoothed Particle Hydrodynamics Method. 5-A, http://dx.doi.org/10.1115/OMAE2022-78419.

Tagliafierro, B., Karimirad, M., Martínez-Estévez, I., Domínguez, J.M., Viccione, G., Crespo, A.J.C., 2022b. Numerical assessment of a tension-leg platform wind turbine in intermediate water using the smoothed particle hydrodynamics method. Energies 15 (11), http://dx.doi.org/10.3390/en15113993, URL: https://www.mdpi.com/1996-1073/15/11/3993.

Tagliafierro, B., Martínez-Estévez, I., Crego-Loureiro, C., Domínguez, J., Crespo, A., Coe, R., Bacelli, G., Viccione, G., Gómez-Gesteira, M., 2022c. Numerical modeling of Moored floating platforms for wave energy converters using DualSPHysics. In: Proceedings of 41^{S}t International Conference on Offshore Mechanics and Arctic Engineering. OMAE, p. 8.

Tagliafierro, B., Martínez-Estévez, I., Domínguez, J.M., Crespo, A.J., Göteman, M., Engström, J., Gómez-Gesteira, M., 2022d. A numerical study of a taut-moored point-absorber wave energy converter with a linear power take-off system under extreme wave conditions. Appl. Energy 311, 118629. http://dx.doi.org/10.1016/j.apenergy.2022.118629, URL: https://www.sciencedirect.com/science/article/pii/S0306261922000988.

Tan, Z., Sun, P.-N., Liu, N.-N., Li, Z., Lyu, H.-G., Zhu, R.-H., 2023. SPH simulation and experimental validation of the dynamic response of floating offshore wind turbines in waves. Renew. Energy 205, 393–409. http://dx.doi.org/10.1016/j.renene.2023.01.081, URL: https://www.sciencedirect.com/science/article/pii/S0960148123000903.

Tasora, A., Serban, R., Mazhar, H., Pazouki, A., Melanz, D., Fleischmann, J., Taylor, M., Sugiyama, H., Negrut, D., 2016. Chrono: An open source multi-physics dynamics engine. ISBN: 978-3-319-40360-1, pp. 19–49. http://dx.doi.org/10.1007/978-3-319-40361-8_2.

Tavakoli, S., Khojasteh, D., Haghani, M., Hirdaris, S., 2023. A review on the progress and research directions of ocean engineering. Ocean Eng. 272, 113617. http://dx.doi.org/10.1016/j.oceaneng.2023.113617, URL: https://www.sciencedirect.com/science/article/pii/S002980182300001X.

Tosdevin, T., Jin, S., Simmonds, D., Hann, M., Greaves, D., 2023. On the use of constrained focused waves for characteristic load prediction. In: C.G., S. (Ed.), Trends in Renewable Energies Offshore - Proceedings of the 5th International Conference on Renewable Energies Offshore, RENEW 2022. CRC Press/Balkema, pp. 609–617. http://dx.doi.org/10.1201/9781003360773-69, URL: https://www.scopus.com/inward/record.uri?eid=2-s2.0-85143426173&doi=10.1201%2f9781003360773-69&partnerID=40&md5=d5383ba80a3b6697fd55d61bfde5d2a3.

Tran, T., Kim, D., Song, J., 2014. Computational fluid dynamic analysis of a floating offshore wind turbine experiencing platform pitching motion. Energies 7 (8), 5011–5026. http://dx.doi.org/10.3390/en7085011, URL: https://www.mdpi.com/1996-1073/7/8/5011.

Tromans, P.S., Anaturk, A.R., Hagemeijer, P., 1991. A new model for the kinematics of large ocean waves-application as a design wave. In: International Ocean and Polar Engineering Conference, All Days. ISOPE-I-91-154.

Vacondio, R., Altomare, C., Leffe, M., Hu, X., Le Touzé, D., Lind, S., Marongiu, J.-C., Marrone, S., Rogers, B., Souto-Iglesias, A., 2020. Grand challenges for Smoothed Particle Hydrodynamics numerical schemes. Comput. Part. Mech. 8, 1–14. http://dx.doi.org/10.1007/s40571-020-00354-1.

van Essen, S., Seyffert, H., 2023. Finding dangerous waves—Review of methods to obtain wave impact design loads for marine structures. J. Offshore Mech. Arct. Eng. 145 (6), http://dx.doi.org/10.1115/1.4056888, arXiv:https://asmedigitalcollection.asme.org/offshoremechanics/article-pdf/145/6/060801/6994784/omae_145_6_060801.pdf. 060801.

Varghese, R., Pakrashi, V., Bhattacharya, S., 2022. A compendium of formulae for natural frequencies of offshore wind turbine structures. Energies 15 (8), http://dx.doi.org/10.3390/en15082967, URL: https://www.mdpi.com/1996-1073/15/8/2967.

Verbrugghe, T., Domínguez, J., Altomare, C., Tafuni, A., Vacondio, R., Troch, P., Kortenhaus, A., 2019. Non-linear wave generation and absorption using open boundaries within DualSPHysics. Comput. Phys. Comm. 240, 46–59. http://dx.doi.org/10.1016/j.cpc.2019.02.003.

Violeau, D., 2012. Fluid Mechanics and the SPH Method: Theory and Applications. OUP Oxford, URL: https://books.google.com/books?id=6uv29S1N6A4C.

Violeau, D., Rogers, B., 2016. Smoothed particle hydrodynamics (SPH) for free-surface flows: past, present and future. J. Hydraul. Res. 54 (1), 1–26. http://dx.doi.org/10.1080/00221686.2015.1119209.

Wang, W., Pákozdi, C., Kamath, A., Martin, T., Bihs, H., 2022a. Hydrodynamic coupling of viscous and nonviscous numerical wave solutions within the open-source hydrodynamics framework reef3d. J. Offshore Mech. Arct. Eng. 144 (4), http://dx.doi.org/10.1115/1.4053848, 041903.

Wang, L., Robertson, A., Jonkman, J., Kim, J., Shen, Z.-R., Koop, A., Borràs Nadal, A., Shi, W., Zeng, X., Ransley, E., Brown, S., Hann, M., Chandramouli, P., Viré, A., Ramesh Reddy, L., Li, X., Xiao, Q., Méndez López, B., Campaña Alonso, G., Oh, S., Sarlak, H., Netzband, S., Jang, H., Yu, K., 2022b. OC6 phase Ia: CFD simulations of the free-decay motion of the DeepCwind semisubmersible. Energies 15 (1), http://dx.doi.org/10.3390/en15010389, URL: https://www.mdpi.com/1996-1073/15/1/389.

Wang, L., Robertson, A., Jonkman, J., Yu, Y.-H., Koop, A., Borràs Nadal, A., Li, H., Bachynski-Polić, E., Pinguet, R., Shi, W., Zeng, X., Zhou, Y., Xiao, Q., Kumar, R., Sarlak, H., Ransley, E., Brown, S., Hann, M., Netzband, S., Wermbter, M., Méndez López, B., 2021. OC6 Phase Ib: Validation of the CFD predictions of difference-frequency wave excitation on a FOWT semisubmersible. Ocean Eng. 241, 110026. http://dx.doi.org/10.1016/j.oceaneng.2021.110026, URL: https://www.sciencedirect.com/science/article/pii/S0029801821013603.

Wang, L., Robertson, A., Kim, J., Jang, H., Shen, Z.-R., Koop, A., Bunnik, T., Yu, K., 2022c. Validation of CFD simulations of the moored DeepCwind offshore wind semisubmersible in irregular waves. Ocean Eng. 260, 112028. http://dx.doi.org/10.1016/j.oceaneng.2022.112028, URL: https://www.sciencedirect.com/science/article/pii/S0029801822013580.

Wei, Z., Edge, B.L., Dalrymple, R.A., Hérault, A., 2019. Modeling of wave energy converters by GPUSPH and Project Chrono. Ocean Eng. 183, 332–349. http://dx.doi.org/10.1016/j.oceaneng.2019.04.029, URL: https://www.sciencedirect.com/science/article/pii/S0029801818317608.

Wendland, H., 1995. Piecewise polynomial, positive definite and compactly supported radial basis functions of minimal degree. Adv. Comput. Math. 4 (1), 389–396. http://dx.doi.org/10.1007/BF02123482, URL: http://sro.sussex.ac.uk/id/eprint/24323/.

Whittaker, C., Fitzgerald, C., Raby, A., Taylor, P., Orszaghova, J., Borthwick, A., 2017. Optimisation of focused wave group runup on a plane beach. Coast.

Eng. 121, 44–55. http://dx.doi.org/10.1016/j.coastaleng.2016.12.001, URL: https://www.sciencedirect.com/science/article/pii/S0378383916304161.

Windt, C., Davidson, J., Ringwood, J.V., 2018. High-fidelity numerical modelling of ocean wave energy systems: A review of computational fluid dynamics-based numerical wave tanks. Renew. Sustain. Energy Rev. 93, 610–630. http://dx.doi.org/10.1016/j.rser.2018.05.020, URL: https://www.sciencedirect.com/science/article/pii/S1364032118303629.

Yan, X., Chen, C., Yin, G., Ong, M.C., Ma, Y., Fan, T., 2023. Numerical investigations on nonlinear effects of catenary mooring systems for a 10-MW FOWT in shallow water. Ocean Eng. 276, 114207. http://dx.doi.org/10.1016/j.oceaneng.2023.114207, URL: https://www.sciencedirect.com/science/article/pii/S0029801823005917.

Yang, Y., Draycott, S., Stansby, P.K., Rogers, B.D., 2023. A numerical flume for waves on variable sheared currents using smoothed particle hydrodynamics (SPH) with open boundaries. Appl. Ocean Res. 135, 103527. http://dx.doi.org/10.1016/j.apor.2023.103527, URL: https://www.sciencedirect.com/science/article/pii/S0141118723000688.

Zeng, X., Shi, W., Feng, X., Shao, Y., Li, X., 2023a. Investigation of higher-harmonic wave loads and low-frequency resonance response of floating offshore wind turbine under extreme wave groups. Mar. Struct. 89, 103401. http://dx.doi.org/10.1016/j.marstruc.2023.103401, URL: https://www.sciencedirect.com/science/article/pii/S0951833923000345.

Zeng, F., Zhang, N., Huang, G., Gu, Q., He, M., 2023b. Dynamic response of floating offshore wind turbines under freak waves with large crest and deep trough. Energy 278, 127679. http://dx.doi.org/10.1016/j.energy.2023.127679, URL: https://www.sciencedirect.com/science/article/pii/S0360544223010733.

Zhang, L., Shi, W., Karimirad, M., Michailides, C., Jiang, Z., 2020. Second-order hydrodynamic effects on the response of three semisubmersible floating offshore wind turbines. Ocean Eng. 207, 107371. http://dx.doi.org/10.1016/j.oceaneng.2020.107371, URL: https://www.sciencedirect.com/science/article/pii/S0029801820304029.

Zhou, Y., Xiao, Q., Liu, Y., Incecik, A., Peyrard, C., Li, S., Pan, G., 2019. Numerical modelling of dynamic responses of a floating offshore wind turbine subject to focused waves. Energies 12 (18), http://dx.doi.org/10.3390/en12183482, URL: https://www.mdpi.com/1996-1073/12/18/3482.